

Yielding under the microscope: a multi-scale perspective on brittle and ductile behaviors in oscillatory shear

Paolo Edera^{1,2,a,b}, Matteo Brizioli^{1,2b}, Mahnoosh Madani^{e,f}, Elie N'gouamba^c, Philippe Coussot^c, Veronique Trappe^d, George Petekidis^{e,f}, Fabio Giavazzi^{2b}, and Roberto Cerbino^g

^aC3M lab, ESPCI ParisTech, 10 rue Vauquelin, 75005 Paris, France; ^bDepartment of Medical Biotechnology and Translational Medicine, University of Milan, Via Fratelli Cervi, 93 - L.I.T.A. Segrate 20054 SEGRATE (MI), Italy; ^cLab. Navier, Ecole des Ponts, Univ. Gustave Eiffel, CNRS, 77420, Champs sur Marne, France; ^dDepartment of Physics, University of Fribourg, Ch. du Musée 3, 1700 Fribourg, Switzerland; ^eFoundation for Research and Technology Hellas, Institute of Electronic Structure and Laser, Road to Voutes, Heraklion 71110, Crete Greece; ^fDepartment of Material Science and Technology, University of Crete, Heraklion 71300, Crete Greece; ^gFaculty of Physics, University of Vienna, Boltzmanngasse 5, A-1090 Vienna, Austria

This manuscript was compiled on February 2, 2024

We study the yielding transition in soft jammed materials under oscillatory shear, employing a novel methodology that combines rheological measurements with detailed dynamical observations. This method provides a comprehensive view of the intricate interactions between macroscopic mechanical behavior, mesoscopic deformation patterns, and microscopic dynamics during yielding. Our findings reveal two distinct yielding behaviors: at one end, a smooth, uniform transition, characterized by homogeneous strain fields, and Fickian, Gaussian microscopic dynamics; at the other, a sharp transition defined by pronounced shear banding, with the dynamics within shear bands being governed exclusively by the local strain, and exhibiting non-Gaussian, cooperative nature. The viscoplastic fragility emerges as a key macroscopic predictor of these intricate behaviors across micro- and meso-scales, providing a new perspective to understand and quantify ductile and brittle yielding in soft materials.

yielding | rheology | oscillatory shearing | shear banding | microscopic dynamics

1. Introduction

The use of heat to transform rigid, solid materials into more malleable, liquid-like phases, dates back to the earliest human civilizations and has been pivotal in technological advancements throughout history, ranging from metal forging to glassblowing. In contemporary material science, and particularly in the study of soft matter, there is also a significant focus on another type of material transformation that resembles the process of heating solids into liquids, yet driven by mechanical forces rather than thermal energy. This phenomenon, known as *yielding*, is a central concept in the physics of soft materials. At the heart of this concept are yield stress materials (YSM), which exhibit a unique dual nature: they behave substantially like solids when at rest, but transition to a fluid-like state under sufficiently large applied force.

This dual nature of YSM attracted considerable attention due to its theoretical implications as well as its key practical relevance (1–5). In the food industry, for example, the behavior of YSM influences the spreadability of condiments and the stability of sauces. In the manufacturing world, the efficient processing of materials such as pastes and gels relies on a deep understanding of the yielding behavior. Consequently, the study of yielding bridges academic research with applied science, playing a critical role in various industries from culinary arts to industrial manufacturing.

Despite the progress made in understanding yielding, the

phenomenon remains only partially understood, largely due to the multi-scale complexity of the processes involved. Yielding involves at least three scales: microscopically, the local structure and mobility under stress of the elementary constituents of the samples; at the mesoscopic scale, the presence of inhomogeneities of the deformation field, normally on length-scales one or two orders of magnitude larger than that of the particles; macroscopically, the mechanical response of the bulk material. Each of these scales presents unique challenges and requires distinct investigative approaches.

Understanding yielding at the macroscopic scale generally begins with classical rheology, which involves studying the deformation and flow of the material. This scale focuses on the bulk properties of the material and on how it responds to applied stress or strain. Of particular relevance for our

Significance Statement

Understanding the yielding transition in yield stress materials is crucial for a wide array of applications, from the flow of toothpaste and paints in consumer products to the stability of gels in food and cosmetic industries. Our study offers a unique multiscale analysis that goes beyond conventional rheological techniques by observing internal structural changes within materials under periodic mechanical deformation. We connect the macroscopic mechanical behavior of materials with their microscopic structural dynamics during yielding, enabling at the same time an accurate characterization of the sample deformation profile. Our findings reveal a complex interplay between brittleness, shear band formation, and features of the shear-induced microscopic dynamics. Demonstrating the non-Gaussian and cooperative nature of particle dynamics during brittle yielding, we advance our understanding of material behavior under dynamic conditions, paving the way for improved material design and a deeper understanding of yielding.

Authors' Contributions: *Conceptualization:* P.E., M.B., V.T., G.P., F.G. and R.C.; *Data curation:* P.E. and M.B.; *Formal analysis:* P.E. and M.B.; *Funding acquisition:* V.T., F.G. and R.C.; *Investigation:* P.E., M.B. and M.M.; *Methodology:* P.E., M.B., V.T., G.P., F.G. and R.C.; *Project administration:* F.G. and R.C.; *Resources:* E.N.; *Software:* P.E. and M.B.; *Supervision:* P.C., V.T., G.P., F.G. and R.C.; *Validation:* P.E., M.B. and M.M.; *Visualization:* P.E. and M.B.; *Writing – original draft:* P.E., M.B., F.G. and R.C.; *Writing – review and editing:* P.E., M.B., M.M., E.N., P.C., V.T., G.P., F.G. and R.C.;

The authors declare no competing interest.

¹P.E. and M.B. contributed equally to this work

²To whom correspondence should be addressed.

E-mail: paolo.edera@espci.fr; matteo.brizioli@unimi.it; fabio.giavazzi@unimi.it

study are oscillatory rheology tests. These tests consist of applying an oscillatory stress or strain to the material and measuring its response. The material response is then generally characterized in terms of storage (G') and loss (G'') moduli, loosely reflecting the elastic and viscous contributions to the material response function.

Amplitude sweep tests are a classical method used to investigate yielding behavior in oscillatory shear. In these tests, the material is subjected to progressively increasing strain (or stress) amplitudes while maintaining a constant frequency. The yield point is typically identified as the transition point where the material response shifts from being predominantly elastic to predominantly viscous. Despite their varied microstructures, most yield stress materials (YSM) display a characteristic behavior in amplitude sweeps, commonly referred to as type-III behavior (Fig. S1 b,c,d) (6). At low strains, the first-harmonic response is dominated by the storage modulus G' , indicating solid-like behavior. As the shear amplitude is increased, an overshoot of G'' , mirroring viscous energy dissipation, is observed. This ultimately culminates in a terminal regime at large strains where G'' becomes dominant, marking the transition of the material to a more liquid-like state.

Differences among type-III materials in oscillatory shear tests are generally observed by considering their higher harmonics response (5, 6). Recent studies have also identified that features of the first-harmonic response can help distinguish between these materials, a notable example being the viscoplastic fragility number (7). This phenomenological quantity quantifies the susceptibility of G'' to strain near yielding: materials exhibiting high viscoplastic fragility demonstrate a rapid transition from solid to liquid state and an accumulation of unrecoverable strain. This characteristic is akin to the stress overshoot observed in steady-shear-startup tests, where the magnitude and abruptness of the stress drop serve as indicators of the material *brittleness* during yielding. It has been suggested that brittle yielding is often associated with *shear banding* – the occurrence of localized zones with distinct shear or strain rates – whereas ductile yielding, especially for athermal systems, shows limited or no shear banding and smaller stress overshoots (8).

Shear banding occurs at the mesoscopic scale and, as such, can not be directly quantified in rheological tests. For this reason, most of the quantitative information collected so far about shear bands is coming either from simulations or from experiments probing the flows across the sample gap during simultaneous rheology experiments (9–13). This combination of macroscopic and mesoscopic information has shed light on a ductile-to-brittle transition (DBT) in YSM, indicating that their yielding behavior can change when variables such as temperature, pressure, density, packing fraction, or even sample preparation protocol are altered (8, 14–19). Simulations have suggested a possible scenario in which the annealing degree of the sample affects the energy landscape's heterogeneity, thereby influencing the yielding behavior: poorly annealed samples with a highly heterogeneous energy landscape exhibit a smooth, ductile yielding transition without shear localization, whereas well-annealed samples with a more homogeneous landscape display an abrupt, brittle yielding transition characterized by significant stress overshoot and strain localization (20, 21).

At the microscopic scale, shear induces structural rear-

rangements, measurable through scattering or microscopy. Both non-oscillatory (22–28) and oscillatory shear experiments (29–36) have been employed, each with distinct findings. In non-oscillatory experiments, especially in continuous shear, challenges arise with transient yielding and the large affine displacements. Oscillatory experiments, employing an echo protocol, overcome these challenges by capturing non-affine displacements each oscillation period at zero strain, revealing a transition from absorbing (closed particle trajectories over one oscillation cycle) to diffusive (open trajectories) states at yielding, which has been studied abundantly both in experiments (24, 29, 30, 33, 35, 37–40) and simulations (18, 21, 41–46).

Recent oscillatory shear experiments have explored the connection between macroscopic strain and microscopic dynamics in repulsive YSM (36). Using the echo protocol to probe non-affine dynamics in reciprocal space, these studies have found two distinct relaxation behaviors: a slow, ballistic relaxation below yielding indicative of a soft solid, and a fast, diffusive relaxation above yielding characteristic of a fluidized state. At intermediate strains, the coexistence of liquid and solid phases is suggested. This behavior has been modeled by drawing an analogy with a liquid-gas phase transition, as in the Van Der Waals model, where the inverse strain amplitude and microscopic relaxation rate play the roles of pressure and volume, respectively, and a sample-dependent parameter termed glassiness is analogous to inverse temperature. The inclusion of quenched disorder in the model further refines the correlation with experimental observations, with abrupt yielding corresponding to samples with high glassiness and low disorder, and smooth yielding to those with low glassiness and high disorder. While 'glassiness' and 'disorder' parameters are key factors in these experiments (36), simulations (20) emphasize 'brittleness' and 'energy heterogeneity', offering a different perspective on material response. In particular, brittle yielding is associated to potential shear banding.

Unfortunately, the lack of access to mesoscopic scale in studies using light scattering (36) limits the ability to fully investigate potential shear banding associated with abrupt, brittle yielding. The simultaneous presence of solid and liquid phases reported in (36) raises important questions about the role and effects of shear bands on microscopic dynamics. Since particle dynamics are expected to show spatio-temporal correlations in scenarios with shear banding (47, 48), it becomes crucial to understand how shear bands influence particle mobility and cooperativity.

To address this problem and gain deeper insight into yielding, we devise a multi-scale experimental approach, akin to that used in simulations. We use a custom-built shear rheometer integrated with a commercial optical microscope (28) to perform combined oscillatory shear and microscopy experiments, simultaneously accessing the three scales relevant to yielding. The stationary nature of oscillatory shear allows for consistent and repeatable measurements of the material mechanical response. At the same time one can access the deformation field at the mesoscopic scale, including shear bands if present, and the microscopic plastic rearrangements of the tracers, by using the echo protocol.

Equipped with this novel experimental setup and methodology, we have performed a series of experiments with different samples, exploring the yielding phenomenon across multiple scales under oscillatory shear conditions.

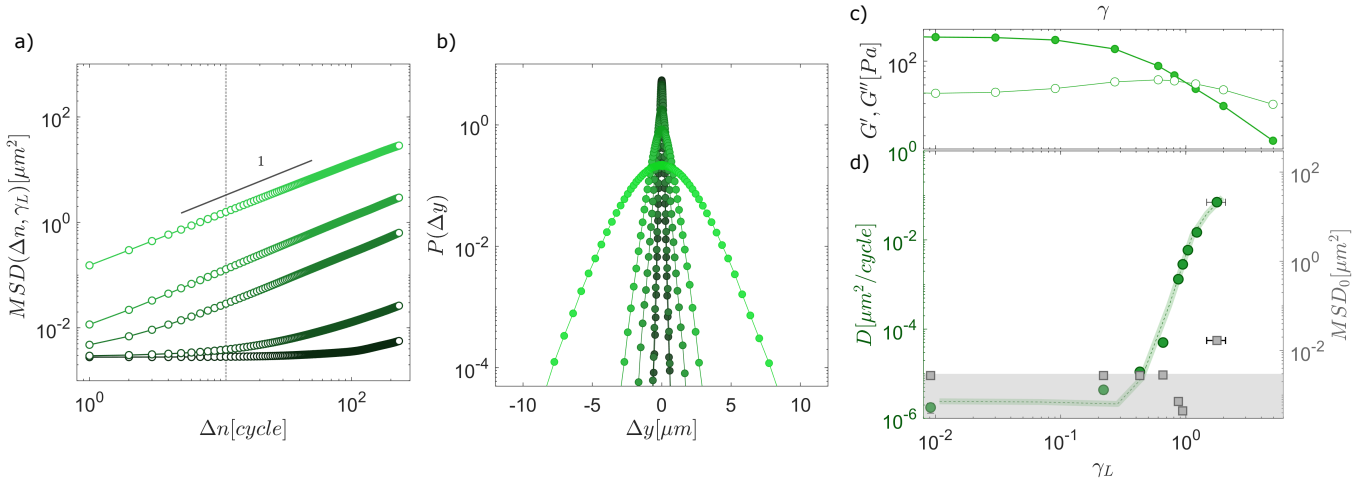


Fig. 1. Homogeneous yielding in Carbopol 5% (a) Stroboscopic mean squared displacement $MSD(\Delta n; \gamma_L)$ for oscillatory shear tests at 1 Hz across different strain amplitudes γ_L (22%, 66%, 87%, 100%, and 177%, with darker to lighter green indicating increasing strains). The MSD is plotted against the number of elapsed cycles (Δn). (b) Probability distribution function (PDF) of tracer displacements in the vorticity direction, shown for $\Delta n = 12$ (corresponding to the vertical dotted line (a)), across the same strain amplitudes. The PDF maintains a Gaussian form for all values of the strain amplitude. (c) Viscoelastic moduli (storage and loss) as a function of imposed strain amplitude, with data representing a stationary state achieved after 120 cycles. (d) With the model in Eq. 2, we fit $MSD(\Delta n; \gamma_L)$ to estimate the initial plateau MSD_0 (gray squares) and the shear-induced diffusion coefficient D (green circles) for each strain amplitude. The shaded area highlights the reliability limits of the measurements.

2. Results and discussion

Our experimental investigation initially focuses on two model systems: a dense dispersion of Carbopol microgels (5 w%) and an oil-in-water emulsion. For the purpose of microscopic investigations, probe particles are dispersed in both systems. Details of the samples characteristics are given in Materials and Methods. Both systems exhibit classical type-III rheology, the yielding transition of the microgel system being smoother than that of the emulsion, as denoted in Fig. 1c and Fig. 4c, respectively. However, exploring the yielding characteristics on the mesoscopic and microscopic length scales reveals much more striking differences between both systems.

A. Ductile yielding in a dense microgel dispersion.

Yielding occurs with homogeneous deformation profiles. To assess the strain profile during oscillatory shear for the dense microgel system, we characterize the stationary displacement field $\Delta x(t, z)$ of the probe particles along the shear direction on different planes, evenly spaced along the vertical (z) direction, according to the methodology established in Refs. (28, 35) and described in more detail in SI. From this data, we estimate the local strain at different positions z along the gap using the equation

$$\gamma_L(z, t) = \frac{\Delta x(z + \frac{\Delta z}{2}, t) - \Delta x(z - \frac{\Delta z}{2}, t)}{\Delta z}, \quad [1]$$

where Δz is the distance between two adjacent planes for which the displacement field has been measured. As shown in Fig. S2 a-c, the yielding transition occurs here with a deformation field that remains homogeneous across the sample gap.

Yielding induces Fickian and Gaussian microscopic dynamics. To assess the dynamics, we use the echo protocol detailed in Refs. (28, 35) using particle tracking (PT), as described in Materials and Methods. The mean square displacement (MSD) of the tracer particles along the vorticity direction (Fig. 1a)

displays linear scaling with increasing number of deformation cycles Δn for all strain amplitudes investigated

$$MSD(\Delta n; \gamma_L) = MSD_0(\gamma_L) + 2D(\gamma_L) \cdot \Delta n, \quad [2]$$

where the short-time plateau MSD_0 corresponds to the PT localization error, substantially independent of strain amplitude (Fig. 1d, grey squares). For larger values of Δn , the linear dependence of the MSD on Δn resembles Fickian dynamics, and can be described by an effective diffusion coefficient $D(\gamma_L)$. As shown in Fig. 1d, $D(\gamma_L)$ becomes measurable well below the crossover point of G' and G'' and exhibits a remarkably strong power-law dependence on strain amplitude $D \sim \gamma_L^\epsilon$, with $\epsilon \simeq 8$ (Fig. 1d, and inset of Fig. 6a). Beyond the linear dependence of the MSD on Δn , we find that the probability distribution functions (PDF) of the particle displacements remain substantially Gaussian across strain amplitudes, as shown in Fig. 1b. The dynamics is thus here best described as Fickian and Gaussian.

An important advantage of our rheo-microscopy method lies in its ability to concurrently access multiple scales. This feature is particularly beneficial when considering data across different experimental runs, which inherently show some small variations. Variability in rheological responses between runs, as those shown in Fig. S7a, often stems from minor differences in cell loading or uncertainties in determining the sample cross-section, as discussed in (28). These variations also impact the microscopic dynamics (Fig. S7c). To account for this, we rescale the strain to $\gamma'_L = \lambda \gamma_L$ where λ is a factor that scales the rheological data to a data set arbitrarily chosen as reference, as shown in Fig. S7b. Remarkably, applying the same rescaling to the microscopic dynamics results again in a master curve (Fig. S7d). This further denotes the value of multi-scale rheo-microscopy used in this work.

Further insight into the shear-induced diffusion mechanism is provided by comparing results with tracers of different sizes. As shown in Fig. 2a, the tracer mobility systematically varies with size, larger particles exhibiting reduced diffusivity. Remarkably, $D \propto 1/a$ as demonstrated by the data collapse

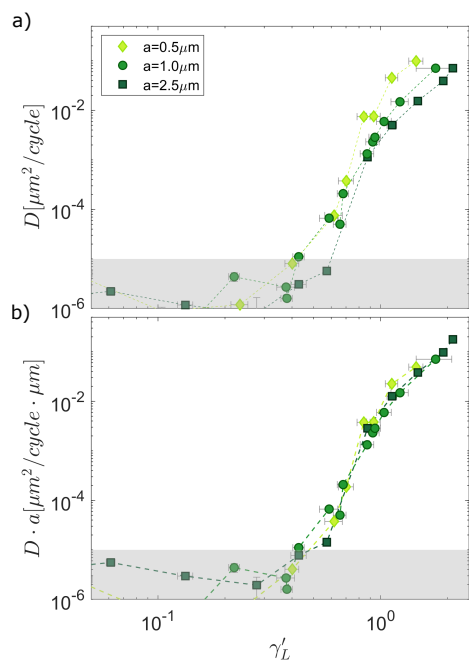


Fig. 2. Shear-induced diffusion of tracers with different sizes adheres to Stokes-Einstein behavior (a) Shear-induced diffusion coefficient for tracers of various radii, as indicated in the legend (\diamond for $a = 0.5 \mu\text{m}$, \circ for $a = 1 \mu\text{m}$, \square for $a = 2.5 \mu\text{m}$), plotted against the rescaled local strain $\gamma'_L = \gamma_L \cdot \lambda$. The factor λ is adjusted for each sample, based on mechanical characterizations, to reduce inter-sample variability (details in the main text and SI). (b) When vertically rescaled by the tracer radius, the data from (a) demonstrate the validity of the Generalized Stokes-Einstein Relation (GSER), which predicts a diffusion coefficient inversely proportional to the tracer radius, $D \propto 1/a$. The shaded areas indicate the reliability limits of the measurements.

obtained by reporting $D \cdot a$ as a function of the local strain (Fig. 2b). This result implies that $D \cdot a$ is an intrinsic descriptor of the shear-induced dynamics, which is strikingly reminiscent of thermal diffusion described by the Stokes-Einstein relation. This is *a priori* surprising, as the motion of the tracer particles are supposedly triggered by the plastic rearrangements occurring within the viscoelastic continuum. At first approximation we would expect that the displacements of the probe particles simply reflect the displacements of the system constituents within the plastically rearranged volume, independent of the particle size. That this is not the case may indicate that the energy responsible for the observed motion is released at a scale smaller than the tracers, akin to thermal Brownian motion. This result is somehow reminiscent of the ideal conditions in passive microrheology experiments, where tracers with size larger than the characteristic length scale of the sample microstructure can accurately probe the local viscoelastic properties of the material and obey a generalized Stokes-Einstein Relation (GSER) (49). In light of this parallel, the observed inverse scaling of the shear-induced diffusion coefficient supports the notion that the shear-induced motions that we study are not merely an artifact of tracer size but rather a genuine representation of the material response to oscillatory shear.

B. Brittle yielding in a dense emulsion.

Yielding occurs with shear banding. For the dense oil-in-water emulsion, yielding leads to a distinctly different behavior. As

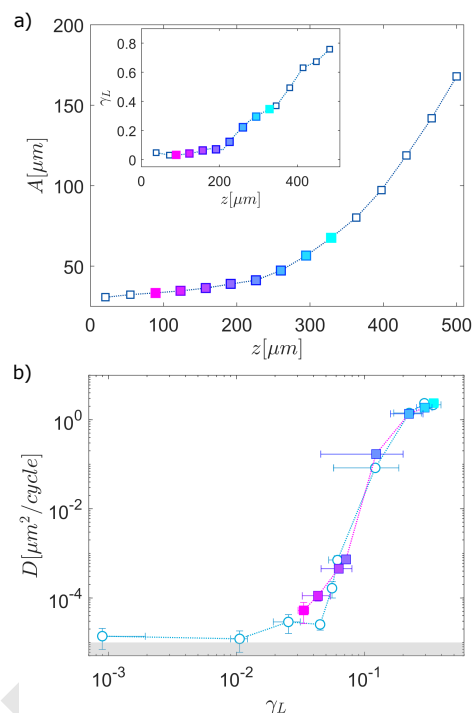


Fig. 3. Correlation of shear-induced diffusion and local strain. In the emulsion, yielding is accompanied by the formation of stationary shear bands. (a) Maximum amplitude $A(z)$ of the displacement $\Delta x(z, t) = A(z) \sin(2\pi\omega t + \phi(z))$, and (in the inset) maximum amplitude $\gamma_L(z)$ of the local strain $\gamma(z, t) = \gamma_L(z) \sin(2\pi\omega t + \phi(z))$, for an imposed maximum strain amplitude $\gamma_0 = 2.5$. (b) Shear-induced diffusion coefficient D as a function of the local strain $\gamma_L(z)$. Blue circles represent data acquired at mid-plane of the shear cell for different nominal strain amplitudes, while squares are from different planes across the gap for a fixed nominal strain amplitude ($\gamma_0 = 2.5$). The color coding in (b) corresponds to that in (a). The data collapse confirms that local strain governs shear-induced dynamics. The shaded area indicates the reliability limits of measurements.

soon the amplitude of the imposed strain is large enough to exceed the linear regime, deviations from a homogeneous deformation field become apparent (Fig. 3a). This is evidenced by the amplitude $\gamma_L(z)$ of the oscillating local strain (Eq. 1) varying with the vertical position (Fig. S2d-f).

Shear-induced diffusion in shear bands is governed by the local strain.

In this system too, the MSD associated with shear-induced dynamics of embedded tracers adheres to the expression in Eq. 2. However, the presence of an inhomogeneous deformation field leads to the tracer mobility, and thus the effective diffusion coefficient, being strongly dependent on the vertical position within the sample gap. Remarkably, we find that the data obtained for varying imposed stress amplitudes at a fixed height directly compares with the data obtained at different height while maintaining the stress amplitude constant, when we consider the local strain as the relevant parameter. As shown in Fig. 3b, graphing D as function of $\gamma_L(z)$ results in a unique master curve for both acquisitions. This finding clearly indicates that the shear-induced dynamics is dictated by local strain rather than the overall stress. It further reveals that the presence of shear bands does not intrinsically alter the nature of the dynamics of the system, but merely alters the magnitude of the diffusion coefficient depending on the local strain conditions.

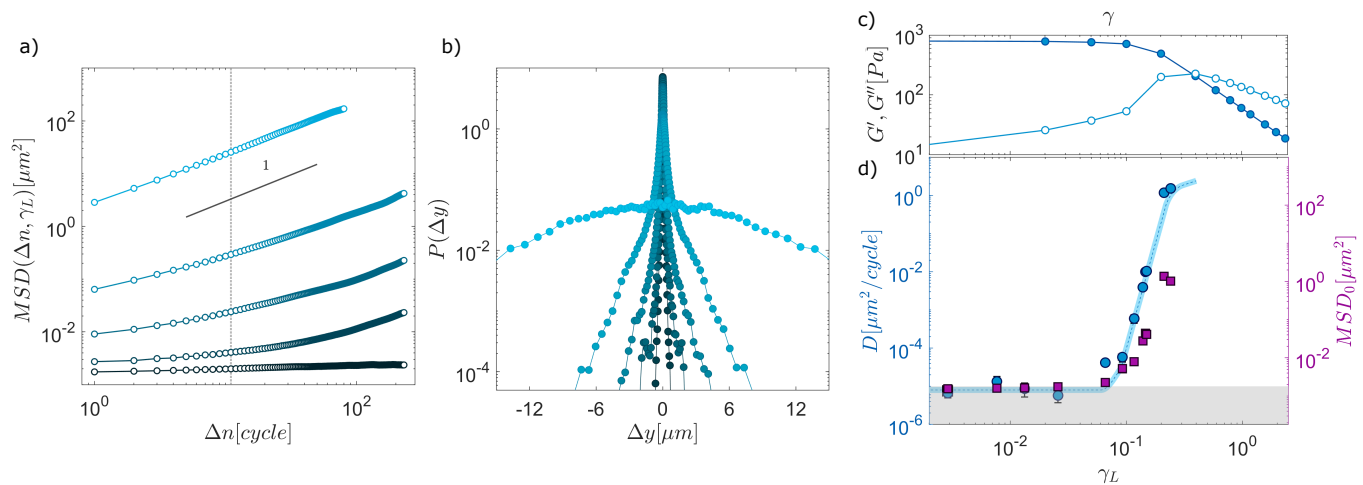


Fig. 4. Heterogeneous yielding for the emulsion. (a) Stroboscopic mean squared displacement (MSD) for oscillatory shear tests at 1 Hz over various local strain amplitudes γ_L (2.6%, 6.6%, 12%, 15%, and 24%, with darker to lighter blue indicating increasing strains). MSD is plotted against the number Δn of elapsed cycles. (b) Probability distribution function (PDF) of tracer displacements along the vorticity direction at $\Delta n = 12$ (matching the vertical dotted line in (a)), for the same γ_L values used in (a). These PDF reveal non-Gaussian tails at most strains, except for the highest values. (c) Results of an amplitude sweep test for the emulsion, conducted under the same testing parameters as in Fig. 1. (d) Fitting the model in Eq. 2 to $MSD(\Delta n; \gamma_L)$, we estimate the shear-induced diffusion coefficient D (blue circles) and initial plateau MSD_0 (purple squares) for each strain amplitude. The shaded area denotes the limits of measurement reliability.

Yielding is accompanied by "reversible plasticity". As noted above, the mean square displacement of the particles embedded in the emulsion displays a simple linear scaling (Fig. 4a), similar to that observed for the microgel system. The effective diffusion coefficient exhibits a power law dependence on the local strain, $D \sim \gamma_L^\epsilon$, with an exponent $\epsilon \simeq 11$ notably larger than that observed for the microgel system (Fig. 4d, and Fig. 6a, inset). Similar to the homogeneous yielding of Carbopol 5%, the diffusive dynamics is observed well below the rheological crossover point (Fig. 4c). However, unlike the homogeneous case, the plateau value $MSD_0(\gamma_L)$ here exceeds the localization noise and becomes strain-dependent for larger γ_L (Fig. 4d). Examination of particle trajectories (Fig. S10) reveals a pattern of *reversible plasticity*, characterized by particles alternating recursively between positions, a phenomenon previously observed in 2D experiments and simulations near yielding transitions (50, 51). This 'jumping' behavior, which is particularly apparent at intermediate strains, leads to heterogeneous motility and manifests as non-Gaussian tails in the displacement PDF (Figs. 4b, S6a and S9).

To further clarify the origin of the short-time plateau MSD_0 , we compare single-particle trajectories in the emulsion to those in Carbopol 5% for strain values leading to the same effective diffusion coefficient D . This comparison (Fig. 5) illustrates well-distinct mobility patterns: rather homogeneous in Carbopol 5%, with little interparticle variability and small fluctuations in single-particle trajectories, and extremely heterogeneous in the emulsion, with large variability in mobility among different tracers, some of them showing intermittent motion and wide positional fluctuations. For small n , this difference becomes larger (Fig. 5b, inset). This indicates that the appearance of a finite MSD_0 for the emulsion is due to intermittently back and forth motion of the particles between different 'metastable' positions. As the strain increases, the actual displacements per cycle increase, such that MSD_0 increases with strain. Quite strikingly, both the diffusion coefficient D and the short-time plateau MSD_0 display Stokes-Einstein like dependence on tracer size, as shown

in Fig. S8.

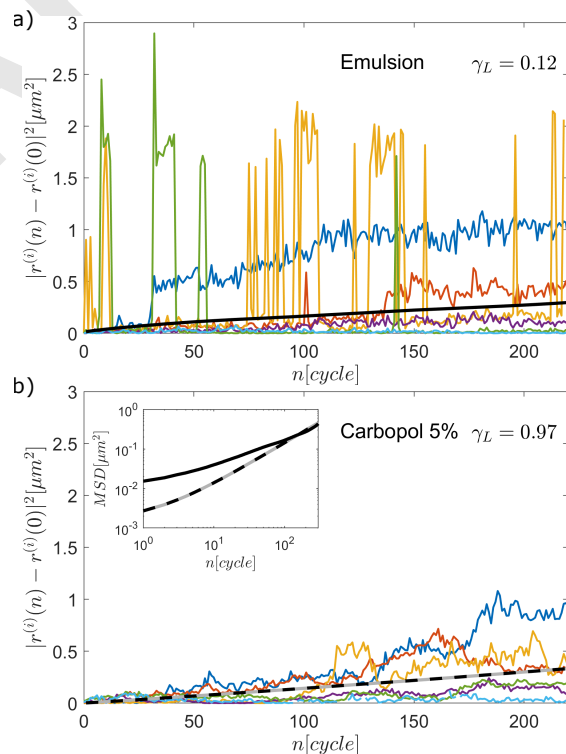


Fig. 5. Origin of the short-time plateau in the mean square displacement. Time-resolved squared displacements of representative particles in two different samples: emulsion (a) and Carbopol 5% (b), selected for their similar effective diffusion coefficients at specific local strain amplitudes ($\gamma_L = 0.12$ for the emulsion and 0.96 for Carbopol 5%). The average mean square displacements calculated over all particles are indicated by a solid line in the emulsion (a) and a dashed line in Carbopol 5% (b), with both also depicted in the inset of (b) for direct comparison. Notably, some trajectories in the emulsion exhibit sudden, reversible jumps, which contribute to the formation of the short-time plateau, as discussed in the main text.

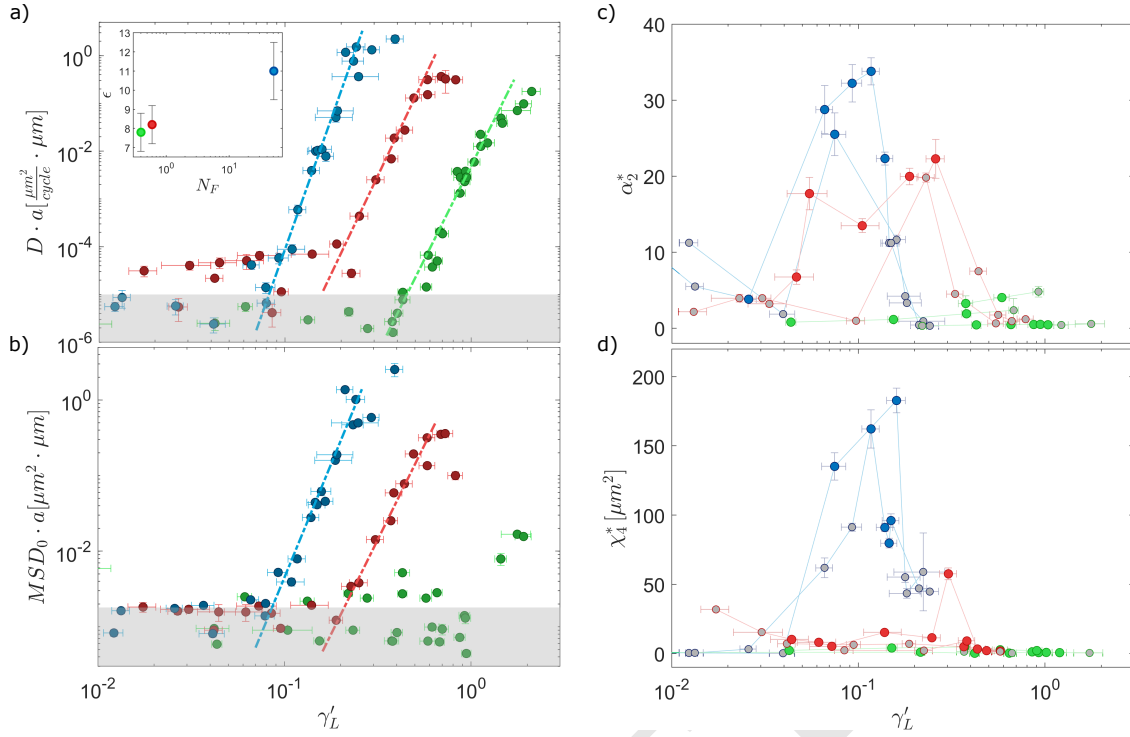


Fig. 6. Comparative analysis of shear-induced dynamics in different materials: emulsion (blue), Carbopol 0.5% (red), and Carbopol 5% (green). (a) Rescaled shear-induced diffusion coefficient $D(\gamma'_L) \cdot a$ plotted against rescaled local strain γ'_L . A strong power-law dependence $D(\gamma'_L) \cdot a \propto \gamma'^{\epsilon}_L$ (dashed lines) is observed at intermediate shear amplitudes. The sample-dependent exponent ϵ is shown in the inset plotted against the viscoplastic fragility number N_F . For Carbopol 0.5%, a sub-linear dependence region is observed at low γ'_L . (b) Rescaled MSD plateau $MSD_0(\gamma'_L) \cdot a$ plotted against the rescaled local strain γ'_L . The dashed lines correspond to power-law scalings $MSD_0 \cdot a \propto \gamma'^{\xi}_L$, with $\xi = 6$ (blue) and 5 (red) for Emulsion and Carbopol 0.5%, respectively. The shaded areas in (a) and (b) indicate the reliability limits of the measurements for D and MSD_0 , respectively. (c) Non-Gaussian parameter maximum $\alpha_2^*(\gamma'_L) = \max_{\Delta n} \{\alpha_2(\Delta n; \gamma'_L)\}$, quantifying deviations from Gaussianity in the PDF of the displacements, plotted as a function of the rescaled local strain γ'_L . The peak value of $\alpha_2^*(\gamma'_L)$ correlates with the brittleness of the sample. (d) Peak of the dynamic susceptibility $\chi_4^*(\gamma'_L) = \max_{\Delta n} \{\chi_4(\Delta n; \gamma'_L)\}$, quantifying the average area of the cooperative rearrangements, as function of the rescaled local strain. In both panels (c) and (d), the points are colored when a peak is observed as a function of the number Δn of elapsed cycles, if no peak is observed the maximum is plotted in grey (the complete Δn dependence is reported in Fig. S6(d-f)). All tests are performed at 1 Hz.

The shear-induced dynamics across heterogeneous yielding is non-Gaussian, and cooperative The observed deviations from Gaussian behavior of the PDF (Fig. 4b), can be quantified using the non-Gaussian parameter, defined as (52, 53)

$$\alpha_2 = \frac{1}{3} \frac{m_4}{(m_2)^2} - 1. \quad [3]$$

where m_n represents the n-th moment of the PDF. For a given strain amplitude, α_2 typically peaks at a number of elapsed cycles Δn corresponding to the strongest deviation from Gaussianity in particle displacements (Fig. S6d). Figure 6c shows the peak value α_2^* for each strain amplitude, highlighting the pronounced non-Gaussian nature of shear-induced displacements in the emulsion compared to Carbopol 5%.

The presence of heterogeneity in the dynamics prompts an investigation of cooperative motion. For this purpose, we evaluate the dynamical susceptibility χ_4 as a function of Δn for each imposed stress (see SI). χ_4 is a parameter widely used to analyze cooperative dynamics in glassy systems (54, 55). Values of χ_4 near zero indicate random, independent displacements, while a pronounced peak in χ_4 signifies heterogeneous dynamics, characterized by spatial clustering of particles with similar mobility. The normalized peak, χ_4^* , provides an estimate of the size of cooperatively rearranging regions within our observational field. The ductile and brittle samples exhibit marked differences in the size of these regions, with a

difference of approximately two orders of magnitude, as shown in Fig. 6d. This finding is in agreement with the idea that dynamics become increasingly correlated at the onset of shear banding (48).

C. Connecting evidence at different length-scales. This section critically discusses how microscopic and mesoscopic observations correlate with the macroscopic features of ductile and brittle yielding transition. To do this, we determine the viscoplastic fragility, which is a phenomenological quantitative indicator of the abruptness of the transition (7). For simplicity, we adopt the following definition of viscoplastic fragility (see also SI):

$$N_F = \max \left[\frac{1}{G''_{lin}} \cdot \frac{\partial G''}{\partial \log \gamma_0} \right], \quad [4]$$

where G''_{lin} is the loss modulus in the linear regime. As shown in the inset of Fig. 6a, N_F , quantifying the rapid increase in macroscopic unrecoverable deformation before the G'' peak, correlates with the power law exponent ϵ that quantifies the increase of the shear-induced diffusivity with increasing strain.

Interestingly, we also observe a robust correlation between ϵ and a key rheological feature beyond the peak of G'' . In this regime, the response is predominantly governed by G'' (with $G'' > G'$), and the loss and storage moduli exhibit specific scaling behaviors: $G'' \propto \gamma_0^{-\nu}$ and $G' \propto \gamma_0^{-2\nu}$ (56),

where ν mirrors the sample sensitivity to strain amplitude. Correspondingly, the stress-strain curve scales as $\sigma_0 \propto \gamma_0^{(1-\nu)}$. When analyzing this scaling for our samples, we find (Fig. S1) that N_F is a monotonically increasing function of ν , which in turn denotes that ϵ is an increasing function of ν . This further denotes that an abrupt yielding transition observed in macroscopic rheology, directly reflects in an abrupt change of the dynamics at the transition.

Our findings further suggest an intriguing connection between the microscopic shear-induced dynamics and the formation of shear bands. To fully assess this relation we study a third sample, Carbopol 0.5%, whose behavior appears intermediate between the two extremes considered so far (Fig. 6). This sample has an intermediate viscoplastic fragility number, and an intermediate power law exponent of the microscopic dynamics (Fig. 6a inset). While its dynamics is non-Gaussian (albeit less pronounced than in the emulsion, Fig. 6c), it is non-cooperative (Fig. 6d), akin to Carbopol 5%. Unlike the emulsion, this sample does not form shear bands (Fig. S2g-i), which further corroborates that shear-induced cooperative motion is directly related to the presence of shear bands at the mesoscopic scale.

3. Conclusion

This work demonstrates the need of using multi-scale approaches to properly assess the characteristics of yielding in different materials. We here use such multi-scale approach to study yielding under oscillatory shear of yield stress materials with different brittleness, brittleness being assessed by the phenomenological viscoplastic fragility number N_F (7). Yield characteristics are simultaneously explored on the macroscopic, mesoscopic and microscopic level, where we use seeded probe particles to measure the deformation fields and the inherent dynamics of the systems under shear.

Independent of brittleness we find that the shear-induced dynamics of the probe particles exhibits features of Fickian diffusion. However, while the particle displacements in the ductile (least brittle) material are Gaussianly distributed, the displacement distributions become increasingly non-Gaussian with increasing brittleness. For the most brittle material, the dynamics eventually exhibits strong spatial correlations, which directly coincides with the formation of shear bands.

The combined determination of strain field and particle dynamics allows us to assess that the shear-induced dynamics in the shear banding sample is exclusively governed by the local strain γ_L . Considering the strain dependence of the particle diffusivity across the yield transition, we find it to exhibit a remarkably strong increase, consistent with $D(\gamma_L) = b \cdot \gamma_L^\epsilon$, where the exponent ϵ is an increasing function of brittleness.

Our unique multi-scale investigation significantly contributes to the understanding of the interplay between macroscopic mechanical responses, shear banding, and microscopic dynamics in soft materials under oscillatory shear. The versatility of our methodology paves the way for examining mechanical properties in a wide array of materials, providing valuable insights for material design and applications in various industrial and biological contexts. The use of dispersed tracers was instrumental in revealing internal deformation processes, often missed in traditional rheological and microscopic studies. Our approach is adaptable even in cases with moderate refractive index mismatches, allowing for plane scanning without tracers.

For significant refractive index contrasts, fluorescent tracers and confocal microscopy could improve axial resolution.

Materials and Methods

Sample preparation. The Carbopol samples were prepared by dispersing Carbopol 971 P NF (purchased by Lubrizol as a single component powder) in MilliQ water to achieve a concentration $c = 5$ wt% for the sample that we refer to as Carbopol 5%. The pH was neutralized by adding a few drops of NaOH while gently stirring for several days. The Carbopol 0.5% sample was obtained by diluting the Carbopol 5% sample with MilliQ water until reaching a concentration $c = 0.5$ wt%. Detailed preparation procedures are described in Ref. (35). The emulsion sample, a concentrated direct (oil-in-water) emulsion (volume fraction: 87%), was prepared by dispersing Dodecane oil in a mixture of water and 3 wt% tetracycltrimethylammonium bromide, following the method detailed in Ref. (57). All samples were seeded with polystyrene colloidal tracers (Microparticles GmbH), selected for compatibility and microscopy contrast, at a concentration of $\phi_t = 0.05\%$. Tracer sizes used were $a_1 = 1 \mu\text{m}$ (for all samples), $a_2 = 2.5 \mu\text{m}$ (for Emulsion and Carbopol 5%), and $a_3 = 0.5 \mu\text{m}$ (for Carbopol 5%). These tracers were evenly dispersed to ensure consistent tracking of internal dynamics during shear deformation. No rheological response difference was observed between samples with and without tracers.

Rheo-microscopy and image analysis. Microscopy tests under shear were performed with a custom-made, stress-controlled shear cell as described in (28). Shear and pre-shear protocols are detailed in SI. Successive movies at different heights were acquired and analyzed as per (28, 35), to characterize deformation profiles $A(z)$ and estimate local deformation γ_L , as described in the main text. An echo strategy was employed to characterize the plastic dynamics of tracers (36), typically focusing on the mid-plane of the gap, unless otherwise specified. In cases of shear banding, acquisitions at different planes, correlating with varying local strains, were compared. The shear-induced trajectories of tracers were reconstructed using a customized MATLAB particle-tracking code (58), available at <https://github.com/dsseara/microrheology>. Mutual displacements were considered to eliminate spurious effects due to global sample drifts or mechanical instabilities. A detailed strategy for eliminating large-scale instabilities is described in SI (Fig. S4, S11). The non-Gaussian parameter $\alpha_2(\Delta n; \gamma'_L)$ (see definitions Eq.S8) quantifies deviations from Gaussianity in the PDF of mutual displacements, varying with imposed strain and number of cycles, and it is both a function of the imposed strain and of the number of elapsed cycles. At the yielding transition $\alpha_2(\Delta n; \gamma'_L)$ has a peak at $\Delta n^*(\gamma'_L)$. In Fig. 6c we report the maximum value of α_2 , which corresponds to the peak $\alpha_2(\Delta n^*(\gamma'_L); \gamma'_L)$, if the peak is present in the observed time window. An analogous argument applies to $\chi_4(\Delta n, \gamma'_L)$ (see SI for further details). Variability between experiments was addressed by rescaling local strains with factors λ , defined in SI, thanks to simultaneous measurements of mechanical response, local deformation, and shear-induced dynamics, allowing for inter-experiment comparisons at all three levels.

Rheology. In addition to utilizing our custom shear cell for rheological measurements, experiments were also conducted using an Anton Paar MCR 501 rheometer in strain-controlled mode, with a cone plate geometry, which offered superior data quality, conserving the homogeneity of the stress field. The period-averaged quantities provided by the instrument software were used for analysis. The results shown in Fig. 3 were obtained with a different shear-cell, described in (35).

Data and software availability. All data in this work have been processed using custom MATLAB codes. These codes, along with representative datasets are publicly available on the Zenodo repository [10.5281/zenodo.10559405](https://zenodo.org/record/10559405). Additionally, videos of the experiments can be made available upon request to the corresponding authors.

ACKNOWLEDGMENTS. We acknowledge useful discussions with Stefano Aime, Ezequiel Ferrero, Stefano Villa, and Giuliano

Zanchetta. We also acknowledge financial support from CNRS (P.E.), from the European Union (G.P., R.C.) through the Twinning project FORGREENSOFT (Number: 101078989 under HORIZON-WIDERA-2021-ACCESS-03), and from Swiss National Science Foundation (V.T., F.G., R.C) Projektförderung (Number: 197340)

Competing Interests

The authors declare that they have no competing interests.

1. A Nicolas, EE Ferrero, K Martens, JL Barrat, Deformation and flow of amorphous solids: Insights from elastoplastic models. *Rev. Mod. Phys.* **90**, 045006 (2018).
2. D Bonn, MM Denn, L Berthier, T Divoux, S Manneville, Yield stress materials in soft condensed matter. *Rev. Mod. Phys.* **89**, 035005 (2017).
3. P Coussot, QD Nguyen, H Huynh, D Bonn, Viscosity bifurcation in thixotropic, yielding fluids. *J. rheology* **46**, 573–589 (2002).
4. L Dahbi, M Alexander, V Trappe, J Dhont, P Schurtenberger, Rheology and structural arrest of casein suspensions. *J. Colloid Interface Sci.* **342**, 564–570 (2010).
5. R Cerbino, V Trappe, Introduction to viscoelasticity and plasticity, and their relation to the underlying microscopic dynamics in soft matter systems. *Phys. A: Stat. Mech. its Appl.* **631**, 128653 (2023).
6. K Hyun, et al., A review of nonlinear oscillatory shear tests: Analysis and application of large amplitude oscillatory shear (laos). *Prog. Polym. Sci.* **36**, 1697–1753 (2011).
7. GJ Donley, PK Singh, A Shetty, SA Rogers, Elucidating the g'' overshoot in soft materials with a yield transition via a time-resolved experimental strain decomposition. *Proc. Natl. Acad. Sci.* **117**, 21945–21952 (2020).
8. HJ Barlow, JO Cochran, SM Fielding, Ductile and brittle yielding in thermal and athermal amorphous materials. *Phys. Rev. Lett.* **125**, 168003 (2020).
9. G Ovarlez, S Rodts, X Chateau, P Coussot, Phenomenology and physical origin of shear localization and shear banding in complex fluids. *Rheol. acta* **48**, 831–844 (2009).
10. R Besseling, et al., Shear banding and flow-concentration coupling in colloidal glasses. *Phys. review letters* **105**, 268301 (2010).
11. T Divoux, D Tamarit, C Barentin, S Manneville, Transient shear banding in a simple yield stress fluid. *Phys. review letters* **104**, 208301 (2010).
12. T Divoux, V Grenard, S Manneville, Rheological hysteresis in soft glassy materials. *Phys. review letters* **110**, 018304 (2013).
13. T Divoux, MA Fardin, S Manneville, S Lerouge, Shear banding of complex fluids. *Annu. Rev. Fluid Mech.* **48**, 81–103 (2016).
14. P Das, AD Parmar, S Sastry, Annealing glasses by cyclic shear deformation. *arXiv preprint arXiv:1805.12476* (2018).
15. H Bhaumik, G Foffi, S Sastry, The role of annealing in determining the yielding behavior of glasses under cyclic shear deformation. *Proc. Natl. Acad. Sci.* **118**, e2100227118 (2021).
16. M Mungan, S Sastry, Metastability as a mechanism for yielding in amorphous solids under cyclic shear. *Phys. review letters* **127**, 248002 (2021).
17. S Sastry, Models for the yielding behavior of amorphous solids. *Phys. Rev. Lett.* **126**, 255501 (2021).
18. JT Parley, S Sastry, P Sollich, Mean-field theory of yielding under oscillatory shear. *Phys. Rev. Lett.* **128**, 198001 (2022).
19. T Divoux, et al., Ductile-to-brittle transition and yielding in soft amorphous materials: perspectives and open questions. *arXiv preprint arXiv:2312.14278* (2023).
20. M Ozawa, L Berthier, G Biroli, A Rosso, G Tarjus, Random critical point separates brittle and ductile yielding transitions in amorphous materials. *Proc. Natl. Acad. Sci.* **115**, 6656–6661 (2018).
21. WT Yeh, M Ozawa, K Miyazaki, T Kawasaki, L Berthier, Glass stability changes the nature of yielding under oscillatory shear. *Phys. review letters* **124**, 225502 (2020).
22. N Koumakis, M Laurati, S Egelhaaf, J Brady, G Petekidis, Yielding of hard-sphere glasses during start-up shear. *Phys. review letters* **108**, 098303 (2012).
23. T Sentjabskaja, et al., Creep and flow of glasses: Strain response linked to the spatial distribution of dynamical heterogeneities. *Sci. reports* **5**, 1–11 (2015).
24. S Aime, L Ramos, L Cipelletti, Microscopic dynamics and failure precursors of a gel under mechanical load. *Proc. Natl. Acad. Sci.* **115**, 3587–3592 (2018).
25. S Aime, L Cipelletti, Probing shear-induced rearrangements in fourier space. i. dynamic light scattering. *Soft matter* **15**, 200–212 (2019).
26. S Aime, L Cipelletti, Probing shear-induced rearrangements in fourier space. ii. differential dynamic microscopy. *Soft Matter* **15**, 213–226 (2019).
27. D Larobina, A Pommella, AM Philippe, MY Nagazi, L Cipelletti, Enhanced microscopic dynamics in mucus gels under a mechanical load in the linear viscoelastic regime. *Proc. Natl. Acad. Sci.* **118**, e2103995118 (2021).
28. S Villa, et al., Quantitative rheo-microscopy of soft matter. *Front. Phys.* p. 905 (2022).
29. P Hébraud, F Lequeux, J Munch, D Pine, Yielding and rearrangements in disordered emulsions. *Phys. Rev. Lett.* **78**, 4657 (1997).
30. G Petekidis, A Moussaid, P Pusey, Rearrangements in hard-sphere glasses under oscillatory shear strain. *physical review E* **66**, 051402 (2002).
31. N Koumakis, J Brady, G Petekidis, Complex oscillatory yielding of model hard-sphere glasses. *Phys. review letters* **110**, 178301 (2013).
32. E Tamborini, L Cipelletti, L Ramos, Plasticity of a colloidal polycrystal under cyclic shear. *Phys. review letters* **113**, 078301 (2014).
33. ED Knowlton, DJ Pine, L Cipelletti, A microscopic view of the yielding transition in concentrated emulsions. *Soft Matter* **10**, 6931–6940 (2014).
34. RL Leheny, MC Rogers, K Chen, S Narayanan, JL Harden, Rheo-xpcs. *Curr. Opin. Colloid & Interface Sci.* **20**, 261–271 (2015).
35. P Edera, et al., Deformation profiles and microscopic dynamics of complex fluids during oscillatory shear experiments. *Soft Matter* **17**, 8553–8566 (2021).
36. S Aime, D Truzzolillo, DJ Pine, L Ramos, L Cipelletti, A unified state diagram for the yielding transition of soft colloids. *Nat. Phys.* pp. 1–7 (2023).
37. P Das, H Vinutha, S Sastry, Unified phase diagram of reversible–irreversible, jamming, and yielding transitions in cyclically sheared soft-sphere packings. *Proc. Natl. Acad. Sci.* **117**, 10203–10209 (2020).
38. NC Keim, PE Arratia, Yielding and microstructure in a 2d jammed material under shear deformation. *Soft Matter* **9**, 6222–6225 (2013).
39. MC Rogers, et al., Microscopic signatures of yielding in concentrated nanoemulsions under large-amplitude oscillatory shear. *Phys. Rev. Mater.* **2**, 095601 (2018).
40. JA Richards, VA Martinez, J Arlt, Characterising shear-induced dynamics in flowing complex fluids using differential dynamic microscopy. *Soft Matter* **17**, 8838–8849 (2021).
41. D Fiocco, G Foffi, S Sastry, Oscillatory athermal quasistatic deformation of a model glass. *Phys. Rev. E* **88**, 020301 (2013).
42. I Regev, T Lookman, C Reichhardt, Onset of irreversibility and chaos in amorphous solids under periodic shear. *Phys. Rev. E* **88**, 062401 (2013).
43. NV Priezjev, Heterogeneous relaxation dynamics in amorphous materials under cyclic loading. *Phys. Rev. E* **87**, 052302 (2013).
44. I Regev, J Weber, C Reichhardt, KA Dahmen, T Lookman, Reversibility and criticality in amorphous solids. *Nat. communications* **6**, 8805 (2015).
45. T Kawasaki, L Berthier, Macroscopic yielding in jammed solids is accompanied by a nonequilibrium first-order transition in particle trajectories. *Phys. Rev. E* **94**, 022615 (2016).
46. P Leishangthem, AD Parmar, S Sastry, The yielding transition in amorphous solids under oscillatory shear deformation. *Nat. communications* **8**, 14653 (2017).
47. L Bocquet, A Colin, A Ajdari, Kinetic theory of plastic flow in soft glassy materials. *Phys. review letters* **103**, 036001 (2009).
48. G Parisi, I Procaccia, C Rainone, M Singh, Shear bands as manifestation of a criticality in yielding amorphous solids. *Proc. Natl. Acad. Sci.* **114**, 5577–5582 (2017).
49. EM Furst, TM Squires, *Microrheology*. (Oxford University Press), (2017).
50. NC Keim, PE Arratia, Mechanical and microscopic properties of the reversible plastic regime in a 2d jammed material. *Phys. review letters* **112**, 028302 (2014).
51. C Reichhardt, I Regev, K Dahmen, S Okuma, C Reichhardt, Reversible to irreversible transitions in periodic driven many-body systems and future directions for classical and quantum systems. *Phys. Rev. Res.* **5**, 021001 (2023).
52. ER Weeks, JC Crocker, AC Levitt, A Schofield, DA Weitz, Three-dimensional direct imaging of structural relaxation near the colloidal glass transition. *Science* **287**, 627–631 (2000).
53. M Brizioli, et al., Reciprocal space study of brownian yet non-gaussian diffusion of small tracers in a hard-sphere glass. *Front. Phys.* p. 408 (2022).
54. P Charbonneau, A Ikeda, G Parisi, F Zamponi, Dimensional study of the caging order parameter at the glass transition. *Proc. Natl. Acad. Sci.* **109**, 13939–13943 (2012).
55. L Berthier, Dynamic heterogeneity in amorphous materials. *Phys. Online J.* **4**, 42 (2011).
56. K Miyazaki, HM Wyss, DA Weitz, DR Reichman, Nonlinear viscoelasticity of metastable complex fluids. *Europhys. Lett.* **75**, 915 (2006).
57. E N'gouamba, J Goyon, P Coussot, Elastoplastic behavior of yield stress fluids. *Phys. Rev. Fluids* **4**, 123301 (2019).
58. V Pelletier, N Gal, P Fournier, ML Kilfoil, Microrheology of microtubule solutions and actin-microtubule composite networks. *Phys. review letters* **102**, 188303 (2009).

PNAS



arXiv:2402.00221v1 [cond-mat.soft] 31 Jan 2024

Supporting Information for

Yielding under the microscope: a multi-scale perspective on brittle and ductile behaviors in oscillatory shear

P. Edera, M. Brizioli, M. Madani, E. N'gouamba, P. Coussot, V. Trappe, G. Petekidis, F. Giavazzi, R. Cerbino

²To whom correspondence should be addressed.

E-mail: paolo.edera@espci.fr; matteo.brizioli@unimi.it; fabio.giavazzi@unimi.it

This PDF file includes:

Supporting text
Figs. S1 to S11
SI References

Supporting Information Text

Rheology experiments with a commercial rheometer

In addition to using our shear cell rheometer, we conducted rheological experiments using an Anton Paar MCR501 rheometer in strain-controlled mode. The experiments used a rough cone and plate geometry with a diameter of 50 mm, which is crucial for ensuring homogeneous deformation fields, especially in the non-linear regime.

During the experiments, a waveform consisting of stress $\sigma(t)$ and strain $\gamma(t)$ data was recorded every two oscillation cycles. For each shear amplitude, we collected 60 experimental waveforms, equivalent to 120 cycles, to ensure comprehensive data coverage. In the non-linear regime, a transient behavior is observed. Our analysis focuses exclusively on data from the stationary regime. The imposed strain is harmonic, while the non-harmonicity of the stress signal is analyzed with a custom code in Matlab as described below.

The stress data represented in the stress-strain curves, $\sigma_0(\gamma_0)$, is sourced directly from the Anton Paar rheometer software, which calculates the amplitude of the first Fourier component of the $\sigma(t)$ signal. Similarly, the viscoelastic moduli reported are those provided by the software, verified to be derived from the amplitude and phase of the first Fourier component of the $\sigma(t)$ signal.

The viscoplastic fragility: In Ref.(1), both storage and loss moduli are decomposed into solid and liquid components, yielding a total of four moduli. The solid components correspond to elastic or recoverable deformations, while the liquid components account for plastic or unrecoverable deformations. This distinction in the loss modulus helps to separate contributions due to plasticity from those due to other dissipation sources present even in the linear regime. From the liquid part of the loss modulus, the viscoelastic fragility is defined as:

$$N_F = \max_{\gamma_0} \left[\frac{1}{G''_{lin}} \cdot \frac{\partial G''_{fluid}}{\partial \log \gamma_0} \right]. \quad [S1]$$

In traditional oscillatory shear experiments, like ours, it is challenging to access these four moduli directly, as separating recoverable and unrecoverable strain is experimentally complex. However, we assume, as in the cases presented by (1), as we are not able to disentangle the recoverable and unrecoverable strain, a procedure that is quite long and tedious experimentally. However, we assume that also for our samples, as in all the cases presented by (1), that G''_{solid} remains nearly constant near the maximum of G''_{fluid} . Given that $\partial \log \gamma_0 G''_{solid} \simeq 0$, it follows that

$$\frac{\partial G''}{\partial \log \gamma_0} \simeq \frac{\partial G''_{fluid}}{\partial \log \gamma_0}. \quad [S2]$$

Therefore, we compute the viscoplastic fragility using the entire loss modulus, introducing only a minor error.

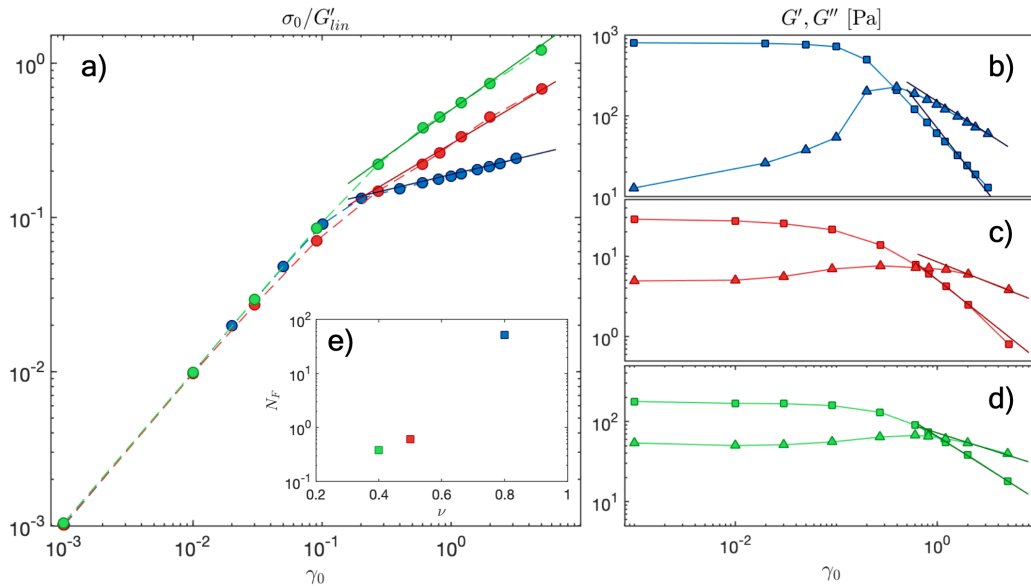


Fig. S1. Rheological characterization of the three samples under oscillatory shear. a) Stress-strain curves, normalized for each sample under oscillatory shear, transitioning from linear to power-law regimes $\sigma_0 \propto \gamma_0^{1-\nu}$. Color coding: emulsion (blue), Carbopol 0.5% wt (red), and Carbopol 5% wt (green). (b-d) Storage and loss moduli (G' , G'') for each sample, demonstrating typical YSM behavior. The exponent ν for the terminal regime is derived from a global fit of the moduli as a function of γ_0 and the stress-strain curves (continuous colored lines). (e) Viscoplastic fragility (N_F) plotted against the terminal flow exponent (ν). The tests are performed in cone plate geometry, ensuring the uniformity of stress throughout all the samples, at a frequency of 1 Hz, with each data point representing a stationary condition achieved after 120 cycles.

Rheomicroscopy experiments with a custom shear cell

A detailed description of the acquisition protocols, processing and analysis of the measurements performed with the custom-built stress-controlled shear cell can be found in refs. (2, 3). Here, we briefly recall some of the acquisition setting parameters, analysis steps, and the most important definitions.

Shear protocol. Before each measurement at a given stress amplitude σ , the initial mechanical properties of the samples were reset by adopting a rejuvenation or preshear protocol. In particular, samples were presheared by imposing an oscillatory stress profile of ~ 400 periods at constant frequency starting from a stress amplitude σ_0 , for which the measured strain amplitude was around $\gamma_0 = 200\text{-}250\%$, reaching the target stress value σ at which the measurement was carried out. After the preshear phase, for each imposed oscillatory stress, we performed 3 acquisitions of duration typically 20-30 oscillation periods from which the strain, hence the rheological response of the material, is estimated. Subsequently, we performed a z-scan with a vertical resolution of Δz of $20\mu\text{m}$, starting from the top-plate and moving downwards to the bottom plate. At each plane, we acquired a fast image sequence of the embedded tracers corresponding to typically 4-5 oscillations. Finally, an echo image sequence was acquired by focusing on the middle plane inside the gap for 400 oscillations.

Imaging settings. Image acquisition was performed with a standard optical microscope (*Nikon Eclipse Ti*), equipped with a 20x, (NA=0.45) objective, keeping the diaphragm completely open (NA=0.52) to minimize the focal depth. Images were acquired with a Ximea MQ042MG-CM USB3.0 camera, with a resolution, upon 2x2 binning, of 512x512 pixels for the z-scan acquisitions and 1024x1024 pixels for the echo sequences. The effective pixel size is $d_{eff} = 0.55\mu\text{m}$. Thanks to an external trigger, the image acquisition is synchronized with the oscillatory stress profile. We imposed an acquisition rate of 45 frames per cycle for the fast z-scan measurements, while we used a frame rate of 10-15 frames per cycle for the echo sequences.

Deformation profiles. As described in refs. (2, 3), the displacement field $\Delta x(z, t)$ is obtained using an image cross-correlation algorithm. We systematically checked that the recorded displacement field is periodic, corresponding to a stationary regime. The local deformation $\gamma_L(z, t)$ is computed as

$$\gamma_L(z, t) = \frac{\Delta x(z + \frac{\Delta z}{2}, t) - \Delta x(z - \frac{\Delta z}{2}, t)}{\Delta z}. \quad [\text{S3}]$$

We note that, while the displacement fields at different heights are not measured simultaneously, we can still compute $\gamma_L(z, t)$ thanks to stationarity, as the origin of the intracycle time t is phase-locked to the applied stress for all heights z . In Fig.S2, we report the amplitude of the deformation profiles $A(z)$ and the estimated local strain amplitude $\gamma_L(z)$ for Carbopol 5% (Fig.S2.a-c), the emulsion (Fig.S2.d-f), and Carbopol 0.5% (Fig.S2.g-i). Repeated measurements on the same sample show that the deformation profile $\gamma_L(z)$ is highly reproducible and time-independent (Fig.S3). However, different independent experiments, involving unloading and reloading fresh samples into the shear cells, yield variable $\gamma_L(z)$ profiles.

Echo image acquisition and analysis

Echo image acquisition. Our echo acquisition scheme consists of capturing a sequence of evenly spaced images covering many oscillation cycles (typically ~ 400). Within each cycle, an integer number n_{echo} (typically ~ 10) of images is captured. In this way, we obtain n_{echo} different stroboscopic image sequences for each experiment (each one corresponding to a different phase of the oscillatory stress), from which we estimate the non-affine dynamics of the embedded tracers. To identify and correct potential drifts in the images due to mechanical instabilities of the experimental setup or to the imperfect synchronization of the acquisition we adopt the following procedure. For each image sub-sequence, we first subtract a background image, obtained as the median of the entire stack, and we then use a rigid registration algorithm exploiting the Image-J plugin Stack-Reg to identify the global translation that potentially occurred between any pair of consecutive echo images. Such transformation is then used to correct frame by frame the tracer positions identified by a particle tracking algorithm, as detailed in the next subsection.

Echo particle tracking. All the results presented in this paper have been obtained by exploiting a customized version of the MATLAB particle-tracking code originally developed in ref. (4) and available online at <https://github.com/dsseara/microrheology>. For each stroboscopic sub-sequence, the tracer positions are identified, drift-corrected as explained in the previous subsection and linked to obtain single particle trajectories $[x^{(i)}(n), y^{(i)}(n)]$ (typically ~ 500).

In what follows, the particle trajectories are investigated in the reference frame of the center of mass. In this reference frame, the spatial average of the velocities $\mathbf{v}^{(i)}(n, \Delta n) = [\frac{x^{(i)}(n+\Delta n) - x^{(i)}(n)}{\Delta n}, \frac{y^{(i)}(n+\Delta n) - y^{(i)}(n)}{\Delta n}]$ of the particles present in the field of view between cycle n and $n + \Delta n$ is identically zero

$$\sum_i^N \mathbf{v}^{(i)}(n, \Delta n) = 0. \quad [\text{S4}]$$

As can be appreciated from Fig.S4.a-c, where representative maps of single particle velocities in the reference frame of the center of mass, spatial correlations are present over the entire image for all the samples. We estimate a characteristic correlation length by considering the velocity-velocity correlation function (5)

$$\Psi(\Delta \mathbf{r}, \Delta n) = \langle V(\mathbf{r} + \Delta \mathbf{r}; n, \Delta n) V(\mathbf{r}; n, \Delta n) \rangle_{n, \mathbf{r}}, \quad [\text{S5}]$$

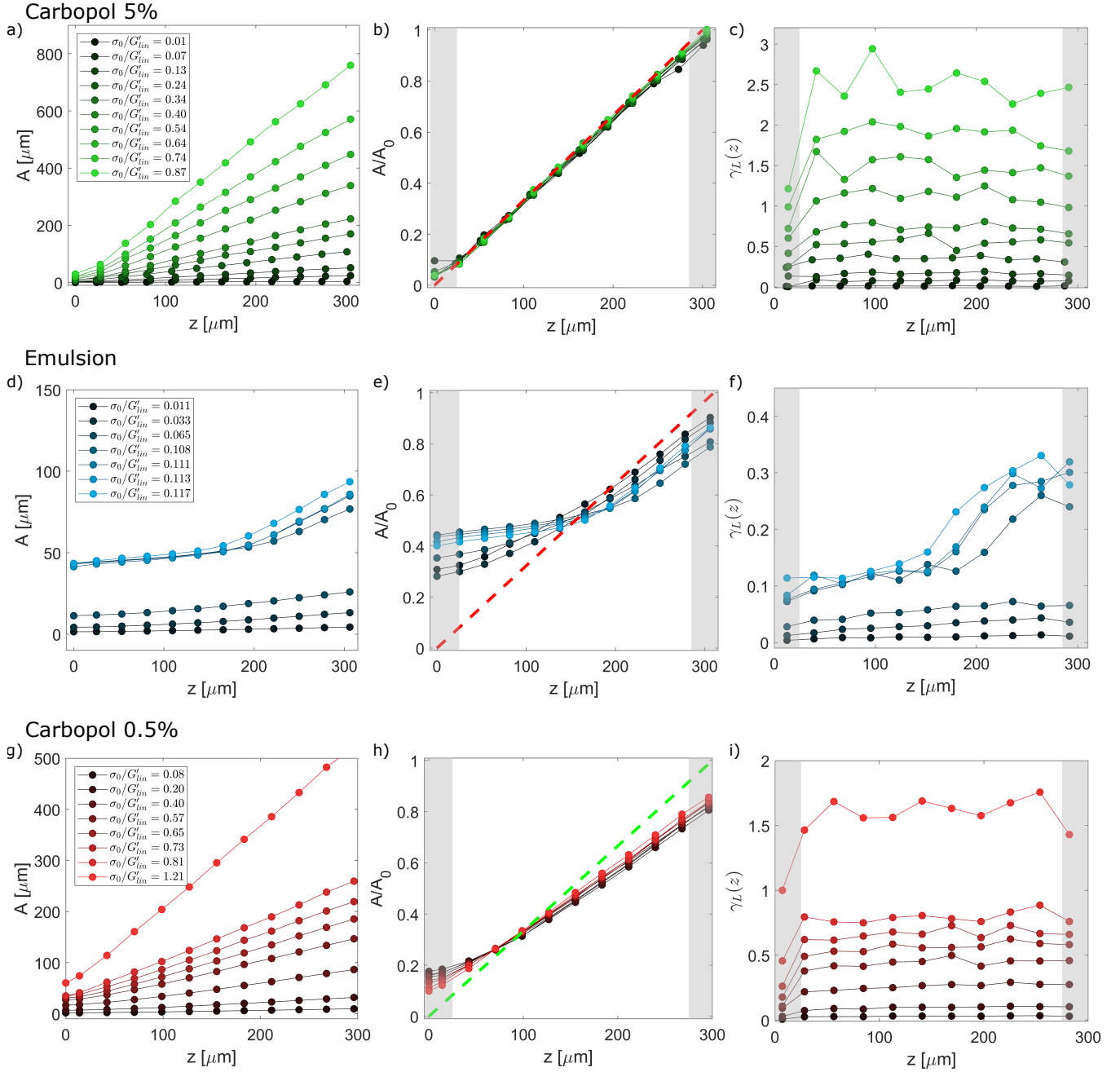


Fig. S2. Deformation profiles and local strain amplitude for Carbopol 5%, emulsion and Carbopol 0.5%. Panels (a-c) refers to Carbopol 5%, panels (d-f) to emulsion and panels (g-i) to Carbopol 0.5%. (a) Deformation profiles $A(z)$ for different imposed stress amplitudes increasing from black to green. (b) Rescaled amplitudes $A(z)$ with the top plate displacement A_0 as measured from the shear-cell(2). The red dashed line stands for the ideal case of a homogeneous profile without shear bands and wall-slip. (c) Effective strain amplitude $\gamma_L(z)$ in the gap estimated exploiting Eq.S3. (d) Representative deformation profile for emulsion. Colors from black to light blue corresponds to increasing stress amplitude. (e) Normalized deformation profile over the bulk deformation A_0 . (f) Estimated strain amplitude $\gamma_L(z)$ across the gap. (g) Representative deformation profile for *Carbopol 0.5%*. Colors ranging from black to red indicates increasing stress amplitude. (e) Normalized deformation profile over the bulk deformation A_0 , with the green dashed line indicating the expected profile in absence of shear-bands and wall-slip. (f) Local strain amplitude $\gamma_L(z)$ across the gap distance.

where $\mathbf{V}(\mathbf{r}; n, \Delta n)$ is defined as: $\mathbf{V}(\mathbf{r}; n, \Delta n) = \sum_{i=1}^N \mathbf{v}^{(i)}(n, \Delta n) \delta(\mathbf{r} - \mathbf{r}^{(i)}(n))$. Representative velocity correlation functions for a fixed number of elapsed cycles Δn are shown in Fig.S4.d-f. For all samples, at short distances, the correlation is positive and then decreases becoming negative at larger distances, with the presence of correlated and anti-correlated domains in all the samples. The presence of at least one zero in the correlation functions is a result of the fact that the average velocity is zero (Eq.S4). The first zero defines a characteristic correlation length that coincides with the average size of the domains. In our case, the occurrences of only two domains (correlated and anticorrelated), with a domain average size of nearly half of the image dimension, suggests the presence of scale-free correlations (5), greater than the typical dimension of the field of view. Since these long-range correlations exceed the typical dimension of our image ROI, we are not able to characterize them.

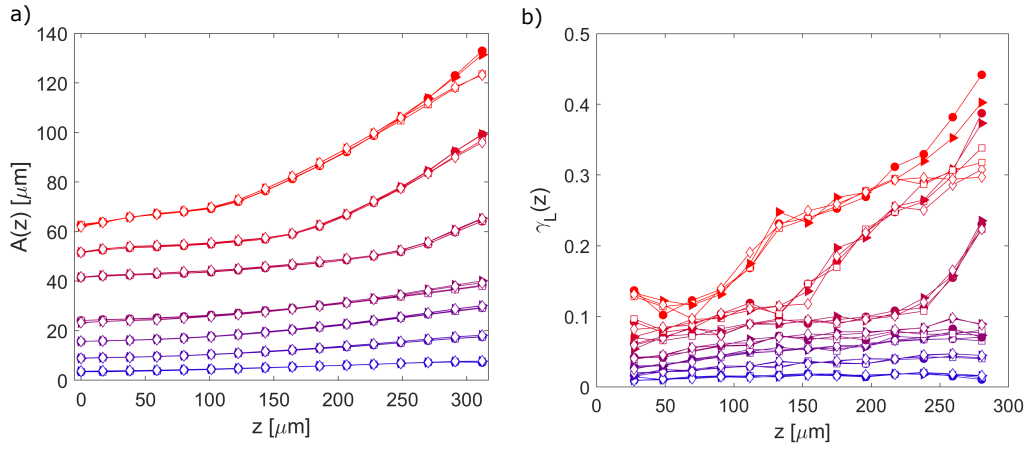


Fig. S3. Assessment of repeatability of deformation profile (a) and strain amplitude (b) for the emulsion. The imposed stress amplitude increase from blue to red. To test the repeatability we performed for each stress amplitude two series of measurements consisting in preshear and subsequent measurements of the deformation profiles by moving downward from the top plate and bottom plate (solid symbols) and then moving upward from the bottom plane to the top one (open symbols). We repeated this protocol two times. Specifically, solid \circ and \triangleright stand for 1st and 2nd downwards, respectively, whereas open \square and ∇ corresponds to 1st and 2nd upwards, respectively.

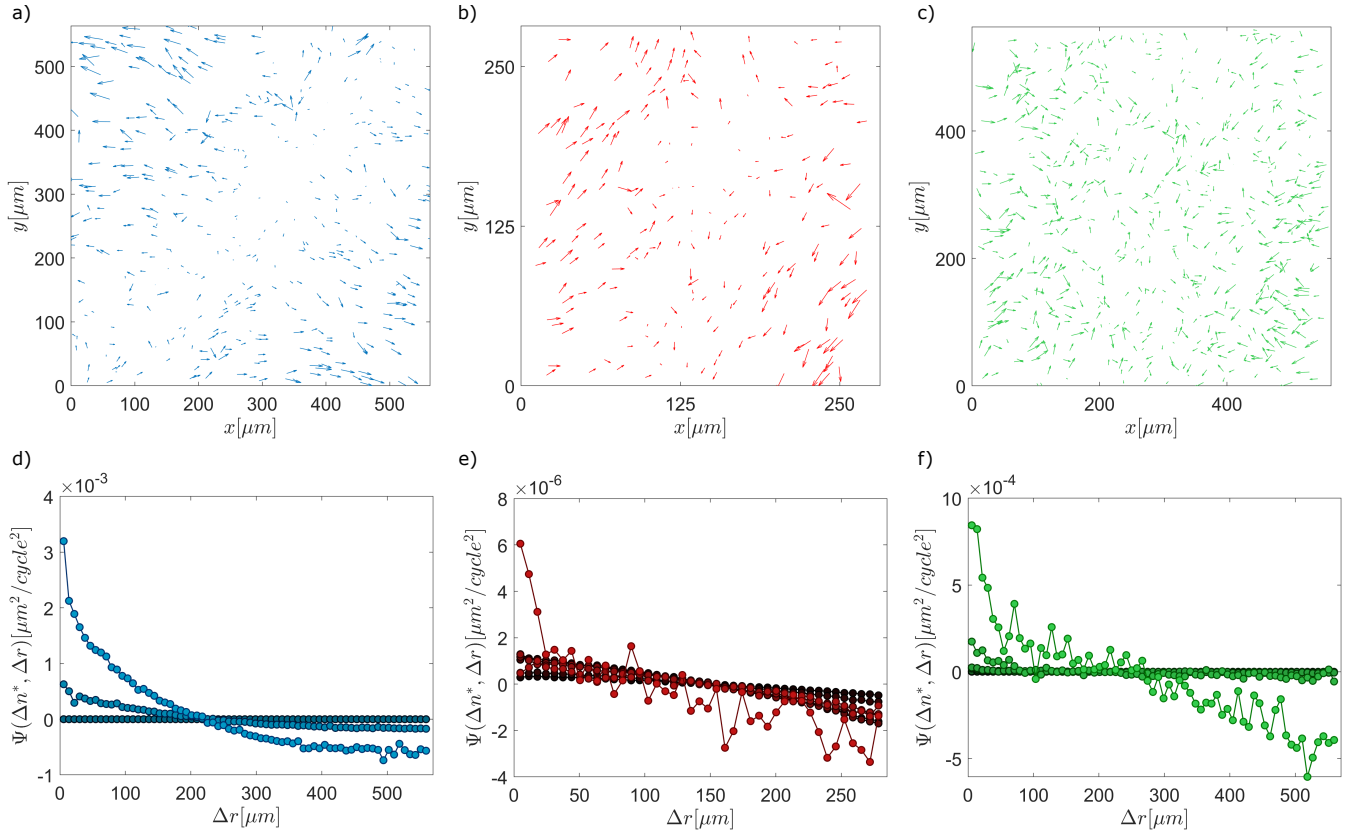


Fig. S4. Velocity Correlations for the three samples. (a-c) 2D projection of the single particles velocities for $\Delta n = 150s$ average over the initial time for $\sigma_0/G'_{lin} \simeq 0.093$ (Emulsion), $\sigma_0/G'_{lin} \simeq 0.27$ (Carbopol 0.5%) and $\sigma_0/G'_{lin} \simeq 0.23$ (Carbopol 5%), respectively. Vectors are scaled for clarity. (d-f) Azimuthally-averaged Velocity correlator $\Psi(\Delta r, \Delta n^*)$ as function of the distance for the three samples, evaluated at Δn^* for which the $\chi_4(\Delta n)$ shows a peak. The different colors indicates different stresses, which increase from the darker to the lighter ones.

These correlated displacements are more or less pronounced depending on the deformation regime, and they can even dominate the MSD in the intermediate amplitude regime. Observations at lower magnification suggest that these flows are due to edge effects, and thus they are not the interest of our study. To characterize the shear-induced dynamics we focus on the *relative* displacement between particles, which is less sensitive to this large-scale correlated motion.

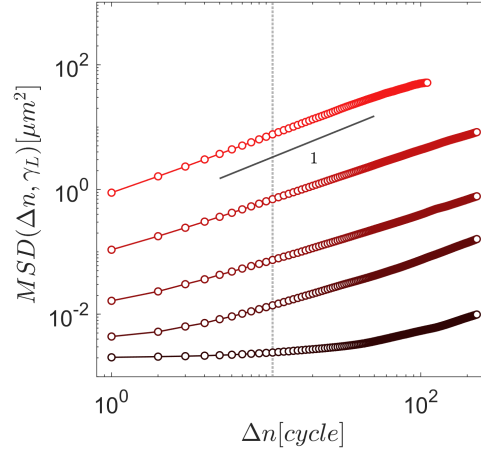


Fig. S5. Mutual mean squared displacement (MSD) for *Carbopol 0.5%* obtained performing oscillatory shear tests at 1 Hz over various local strain amplitudes γ_L (1.8%, 25%, 30%, 44%, and 73%, with darker to lighter blue indicating increasing strains). MSD is plotted against the number Δn of elapsed cycles.

Quantification of the non-affine dynamics

MSD and non-Gaussian parameter. To obtain information on the non-affine particle motion removing possible contributions from long-ranged correlated flows, we adopted a relative particle tracking approach (6), which consists of the study of the relative positions between pairs of particles (i, j), whose relative distance is lower than a characteristic distance $|\Delta r| = 50 \mu\text{m}$ that we set by looking at the particle displacement correlations. In this way, we can define the mean squared displacement (MSD) computed over the relative position of the particles $[\Delta x^{(i,j)}, \Delta y^{(i,j)}] = [x^{(i)}(n) - x^{(j)}(n), y^{(i)}(n) - y^{(j)}(n)]$, along the vorticity direction as

$$MSD(\Delta n) = \frac{1}{2} \langle |\Delta y^{(i,j)}(n + \Delta n) - \Delta y^{(i,j)}(n)|^2 \rangle, \quad [S6]$$

where the average is performed over all pairs of particles and initial cycles. The MSD for a given stress amplitude is then computed by averaging over all the echo phases. We report in Fig.S5 the obtained MSD for *Carbopol 0.5%*.

Similarly, from the relative position of the tracers, we evaluate the particle relative displacement probability distribution functions (PDF) along the vorticity $P(\Delta y, \Delta n)$ direction:

$$P(\Delta y, \Delta n) = \langle \delta[\Delta y - (\Delta y^{(i,j)}(n + \Delta n) - \Delta y^{(i,j)}(n))] \rangle, \quad [S7]$$

where δ is the Dirac's delta function. Representative PDFs at a given time for different imposed stresses are shown in Fig.S6.a-c. As can be noticed, the tails of the PDFs for the case of the emulsion and the *Carbopol 0.5%* are highly non-Gaussian. In order to properly quantify non-Gaussianity, we estimated the one-dimensional non-Gaussian parameter α_2 as:

$$\alpha_2(\Delta n) = \frac{1}{3} \frac{\langle |\Delta y^{(i,j)}(n + \Delta n) - \Delta y^{(i,j)}(n)|^4 \rangle}{\langle |\Delta y^{(i,j)}(n + \Delta n) - \Delta y^{(i,j)}(n)|^2 \rangle^2} - 1. \quad [S8]$$

The non-Gaussian parameter as a function of the elapsed cycles, for different imposed stresses, is reported in Fig.S6.d-f.

Definition of the scaling factor λ . As mentioned in the main text, independent repetitions of the same experiment upon removing from the cell and re-loading a given sample result in slight variations of both macroscopic and microscopic variables (Fig.S7 a-c). Concerning G' and G'' , different experiments requires the introduction of a shift factor $\beta \sim 1$ along the vertical axes, this is the consequence of an error in the sample section measurement and ultimately in the conversion from force to stress. The vertical rescaling is not sufficient to lead to a perfect collapse of the data, a further sample-dependent horizontal scaling factor λ is introduced to correct for minor discrepancy that can be attributed to sample-to-sample variability. When represented against the rescaled variable $\gamma'_L = \lambda \cdot \gamma_L$ the overlap of the data is optimized both for diffusion coefficient and for the dynamic moduli S7 b-d.

Stokes-Einstein-like dependence of the shear-induced diffusion coefficient on the tracer radius for the emulsion. Similarly to the case of homogeneous yielding, the tracer's shear-induced diffusivity in the emulsion displays the same Stokes-Einstein-like dependence on the tracer radius $D \sim 1/a$, and, surprisingly, MSD_0 also shows the same systematic dependence on the radius $MSD_0 \sim 1/a$ (S8). As pointed out in the main text, this behavior is similar to the Generalize-stokes-Einstein relation (GSER). It indicates that the MSD is strictly related to the effective properties of the materials. We stress that the absence of any motion of the tracers in the quiescent state, along with the stoke-Einstein-like dependence of the mobility on the radius suggests that all the tracer sizes employed in this work are larger than the characteristic microstructural scales of the material. In a previous study (3), we investigated the mobility of smaller tracers with radius $a < 0.25 \mu\text{m}$ in similar materials observing thermal motion at rest.

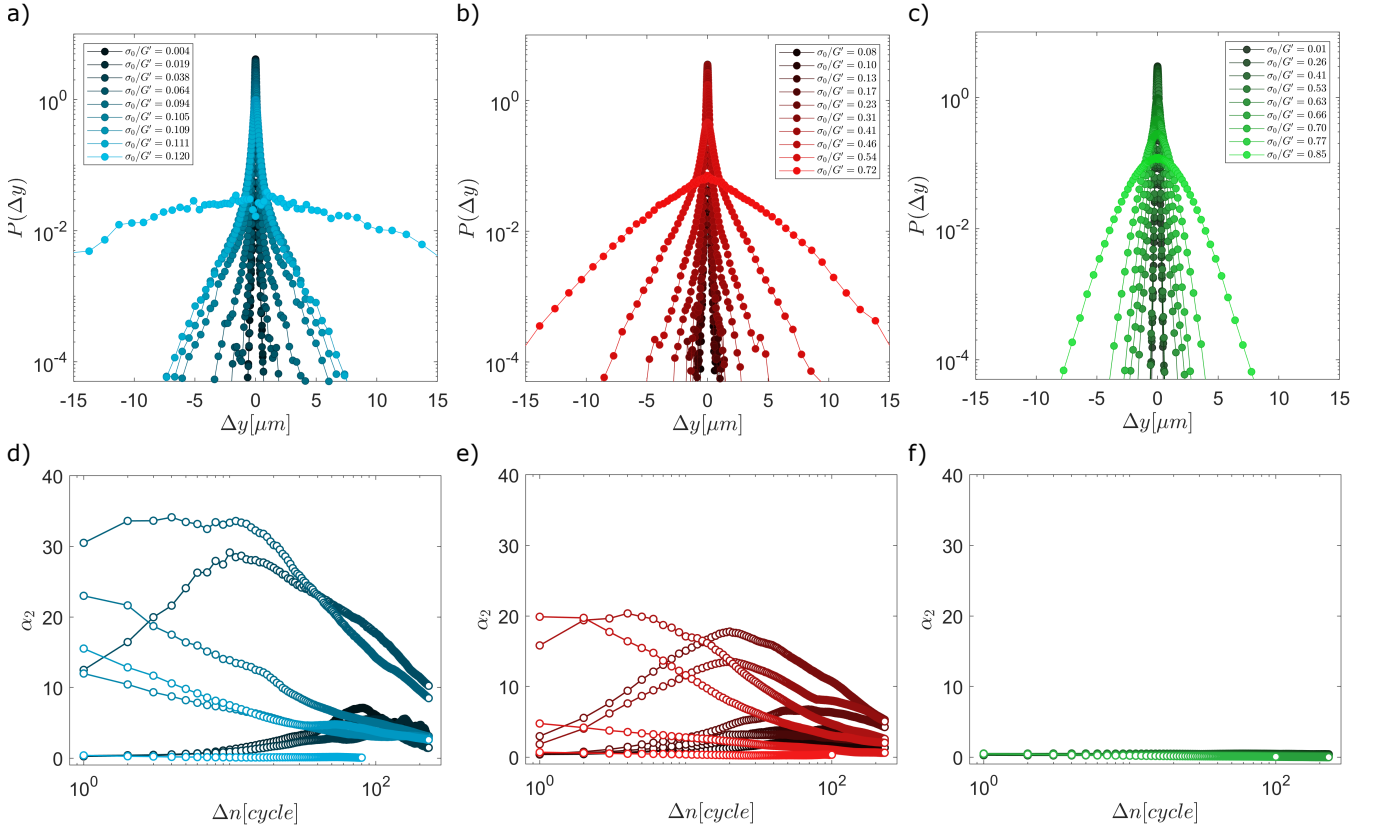


Fig. S6. a-c) Mutual-displacement probability distribution functions for the three samples along the vorticity direction for $\Delta n = 12$ and different stresses. Colors goes from darker to lighter as the stress increases. d-f) Mutual non-gaussian parameter as a function of time for different applied stress $\alpha_2(\Delta n, \gamma_L^*)$. In the main text are reported $\alpha_2^*(\gamma_L^*)$: the values at the peak, when this is observed, or the maximum for a fixed stress/strain.

Despite the Stokes-Einstein-like behavior for the *MSD*, we observe that the pdf of tracer displacement changes qualitatively with the tracer size, indicating that particles of different sizes could display distinct behaviors when higher-order indicators are considered, like, for example, the non-Gaussian parameter α_2 . Specifically, if we consider the case of the emulsion, we observe that the distribution for particle of radius $a = 2.5 \mu\text{m}$ (purple squares) and $a = 1.0 \mu\text{m}$ (Fig.S9.b-c) are different, even considering a condition of similar mobility, hence, the rescaled (by the radius) *MSDs* are almost identical (Fig.S9.a). Inspection of the distribution probability for the smaller tracers reveals a highly dispersed behavior, with a central region (for small displacements) evolving slowly with the number of elapsed cycle Δn as compared to the tails. By contrast, the PDFs for the larger tracers exhibits a more regular behavior with the distribution all broadening over Δn while still remaining highly non Gaussian. This suggests that the smaller particles are more sensitive to the heterogeneity of the material. However, quite remarkably, despite the difference in the details of the distributions, the *MSD* (the variance of the distribution) appears to be independent from these details. This reinforce our claim regarding the *MSD* as a descriptor of the material's effective properties. In addition, we checked that the χ_4 peak values and their behaviors as a function of the strain amplitude for the bigger tracers is similar to those of the smaller tracers the one of the smaller tracers. Therefore, as for the mean squared displacement also the χ_4 is independent of the tracer size and is closely connected to the material properties.

Dynamic heterogeneity. As shown in Fig.S10.a-c, tracer particles can display a broad spectrum of behaviors, with trajectories differing widely from each other under the same applied stress. In particular, some particles display highly intermittent displacements, with localized sudden jumps, while other particles are nearly immobile. This is a first indication of the presence of dynamic heterogeneity and temporal intermittency, which can be quantitatively captured by considering high-order temporal and spatial correlations(7). To quantify the correlations in real space, one can define a *mobility field* $c(\mathbf{r}; n, \Delta n)$ for a system of N particles, as

$$c(\mathbf{r}; n, \Delta n) = \frac{1}{N} \sum_{i=1}^N o^{(i)}(n, \Delta n) \delta(\mathbf{r} - \mathbf{r}^{(i)}(n)), \quad [\text{S9}]$$

where $o^{(i)}(n, \Delta n)$ is an overlap function, which quantifies how much a particle has moved along the vorticity direction between cycle n and $n + \Delta n$

$$o^{(i)}(n, \Delta n) = \exp\left\{-\frac{(y^{(i)}(n + \Delta n) - y^{(i)}(n))^2}{d^2}\right\}, \quad [\text{S10}]$$

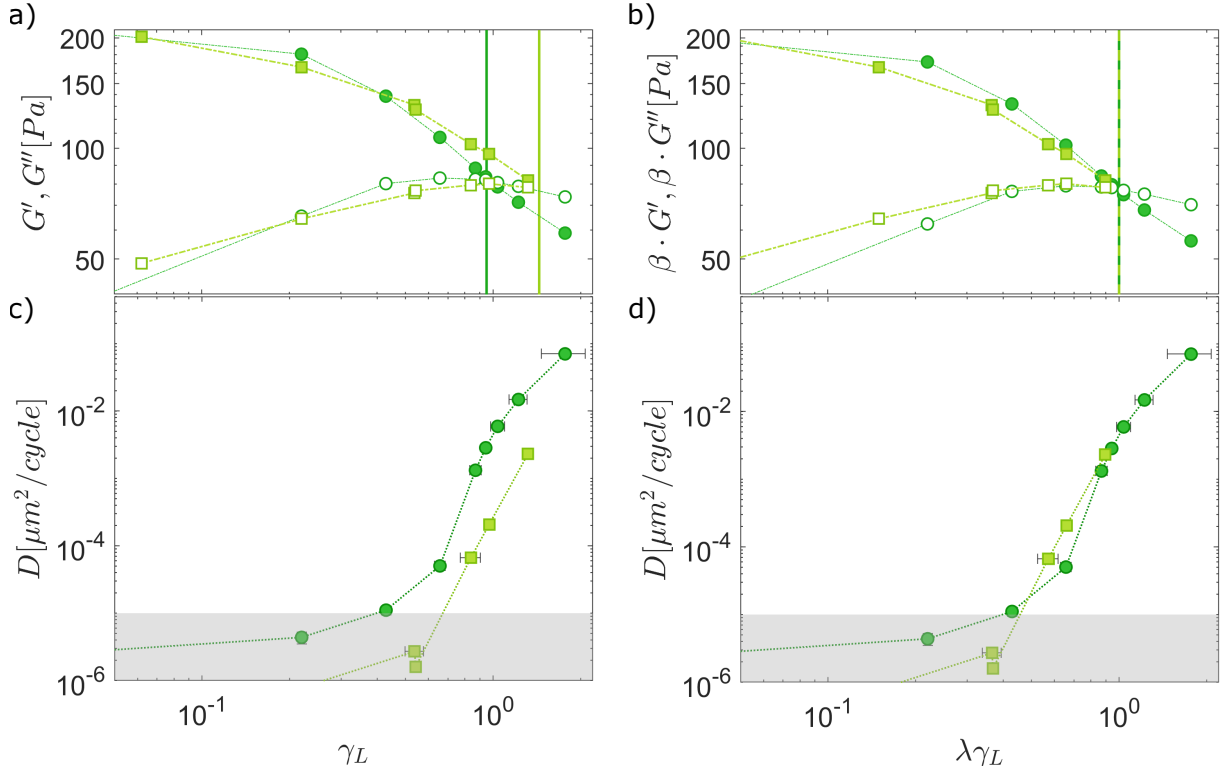


Fig. S7. Definition of the rescaled strain γ'_L . (a) Viscoelastic moduli (a) and diffusion coefficient (b) obtained from two different loadings of the same sample (circles and squares, respectively). In this case Carbopol 5%. The continuous lines in (a) indicate the strain amplitudes γ_L of the crossover points of G' and G'' for the two different repetitions, light green for squares and dark green for circles. (c) Same data of (a) horizontally rescaled by λ . The moduli are also rescaled vertically by a factor $\beta \simeq 1$. (d) Diffusion coefficient as a function of the rescaled strain amplitude $\gamma'_L = \lambda \cdot \gamma$. All the measurements have been performed at $\omega = 2\pi$ [rad/s]

with d being a characteristic distance, typically of the order of the particle size. The degree of the dynamic heterogeneity can be defined as the deviation from the average behavior of the particle mobility. Therefore by defining the total mobility $C(n, \Delta n) = \int d^2 \mathbf{r} c(\mathbf{r}; n, \Delta n)$, we can compute its variance to get the dynamic susceptibility $\chi_4(\Delta n)$:

$$\chi_4(\Delta n) = N[\langle C(n, \Delta n)^2 \rangle - \langle C(n, \Delta n) \rangle^2], \quad [\text{S11}]$$

which is a measure of the degree of dynamic heterogeneity. Although computationally very efficient, this definition of $\chi_4(\Delta n)$ is based on a single-particle approach and it is strongly affected by the presence of long-range correlations in the displacement field, which could lead to an overestimate of $\chi_4(\Delta n)$.

The dynamic susceptibility can be also computed starting from the 'four-point' dynamic correlation function:

$$G_4(\Delta \mathbf{r}, \Delta n) = \langle c(\mathbf{r} + \Delta \mathbf{r}; n, \Delta n) c(\mathbf{r}; n, \Delta n) \rangle_{n, \mathbf{r}} - \langle c(\mathbf{r}; n, \Delta n) \rangle_{n, \mathbf{r}}^2, \quad [\text{S12}]$$

which measures the spatial and temporal correlations between pairs of particles at a certain separation distance $\Delta \mathbf{r}$ and for a certain number of elapsed cycles Δn . By integrating over the separation distance $\Delta \mathbf{r}$, we can retrieve the dynamic susceptibility:

$$\chi_4(\Delta n) = \int d^2 \Delta \mathbf{r} G_4(\Delta \mathbf{r}, \Delta n). \quad [\text{S13}]$$

In this work, the presence of large-scale velocity correlations (Fig.S10.d-f), prevents the correlator $G_4(\Delta \mathbf{r}, \Delta t)$ (Fig.S11.a-c) decaying to zero for large distances, as one would have expected. To correct for this effect in the evaluation of the $\chi_4(\Delta n)$, we subtracted a baseline to the four point correlator obtained by averaging over distances for which it has a plateau, (typically for $r > 200 \mu\text{m}$). The so-obtained new correlator is then integrated using Eq. S13 to get a χ_4 cleaned from spurious correlations (fig.S11d-f):

$$\chi_4(\Delta n) = \int d^2 \Delta \mathbf{r} [G_4(\Delta \mathbf{r}, \Delta n) - G_4(\Delta \mathbf{r} > 200 \mu\text{m}, \Delta n)]. \quad [\text{S14}]$$

For all the experiments in this work, we set $d = 0.15 \mu\text{m}$ as the characteristic distance for the evaluation of the overlap parameter. This value has been chosen by considering different distances d in a range from $0.01 \mu\text{m}$ to $1.0 \mu\text{m}$ and taking the value of d for which the $\chi_4(\Delta n)$ was maximum, together with, the condition of the existence of an interval around d for which $\chi_4(\Delta n)$ exhibited no change in the functional form with Δn . Finally, to compare different experiments and samples, we normalized the χ_4 with the surface density of the particles ϕ in the field of view.

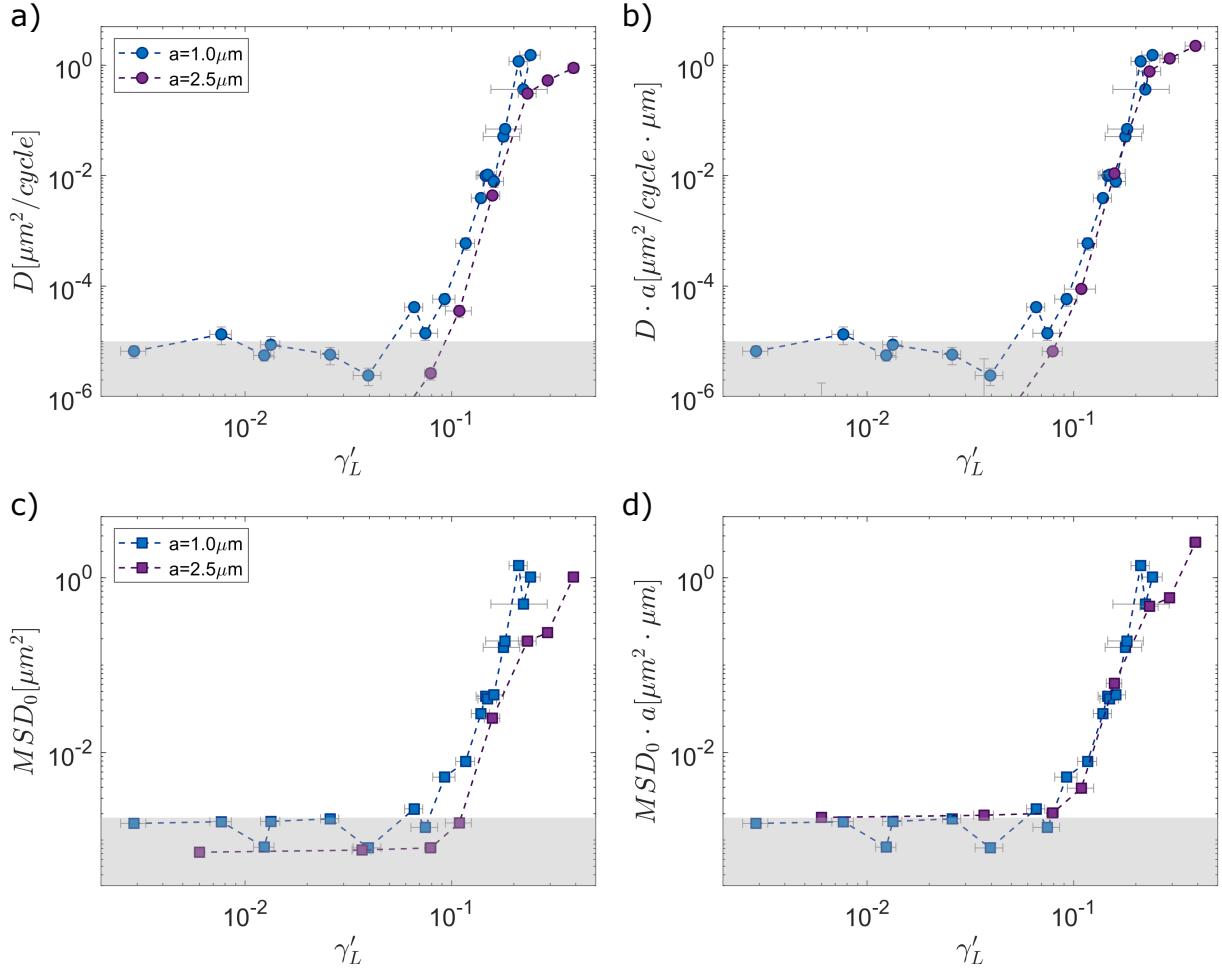


Fig. S8. GSER relation for emulsion. Diffusion coefficient D (a) and MSD_0 (c) as a function of the local strain amplitude γ'_L for two different tracer radius $a = 1 \mu\text{m}$ (blue circles) and, $2.5 \mu\text{m}$ (purple circles). (b,d) Same data as in (a,c) vertically rescaled with the tracer's radius. All the measurements have been performed at $\omega = 2\pi$ rad/s.

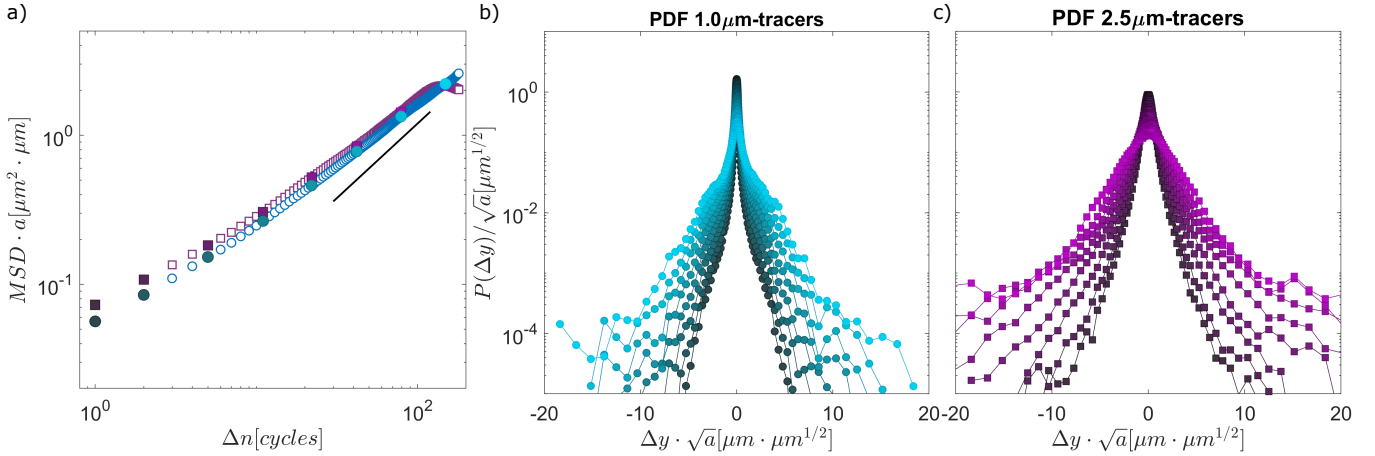


Fig. S9. emulsion. (a) Shear induced MSD rescaled with tracers' radius. Large circles (squares) correspond to Δn whose PDFs are shown in panels (b) and (c). The black line has slope 1 and indicates a diffusive behavior. Representative distribution probability for different number of elapsed cycles (increasing from darker to lighter colors) of two different echo-experiments performed exploiting tracers size (c) $a = 2.5 \mu\text{m}$ (purple squares) and (b) $a = 1.0 \mu\text{m}$ (blue circles). The mobility for the two selected acquisitions is almost the same, as can be observed from the MSD in (a). Specifically, the local strains are $\gamma'_L = 0.15$ and $\gamma'_L = 0.16$ for (b) and for (c), respectively. All the measurements have been performed at $\omega = 2\pi$ rad/s.

References

1. GJ Donley, PK Singh, A Shetty, SA Rogers, Elucidating the g'' overshoot in soft materials with a yield transition via a time-resolved experimental strain decomposition. *Proc. Natl. Acad. Sci.* **117**, 21945–21952 (2020).

2. S Villa, et al., Quantitative rheo-microscopy of soft matter. *Front. Phys.* p. 905 (2022).
3. P Edera, et al., Deformation profiles and microscopic dynamics of complex fluids during oscillatory shear experiments. *Soft Matter* **17**, 8553–8566 (2021).
4. V Pelletier, N Gal, P Fournier, ML Kilfoil, Microrheology of microtubule solutions and actin-microtubule composite networks. *Phys. review letters* **102**, 188303 (2009).
5. A Cavagna, et al., Scale-free correlations in starling flocks. *Proc. Natl. Acad. Sci.* **107**, 11865–11870 (2010).
6. W Pönisch, V Zaburdaev, Relative distance between tracers as a measure of diffusivity within moving aggregates. *The Eur. Phys. J. B* **91**, 1–7 (2018).
7. L Berthier, Dynamic heterogeneity in amorphous materials. *arXiv preprint arXiv:1106.1739* (2011).

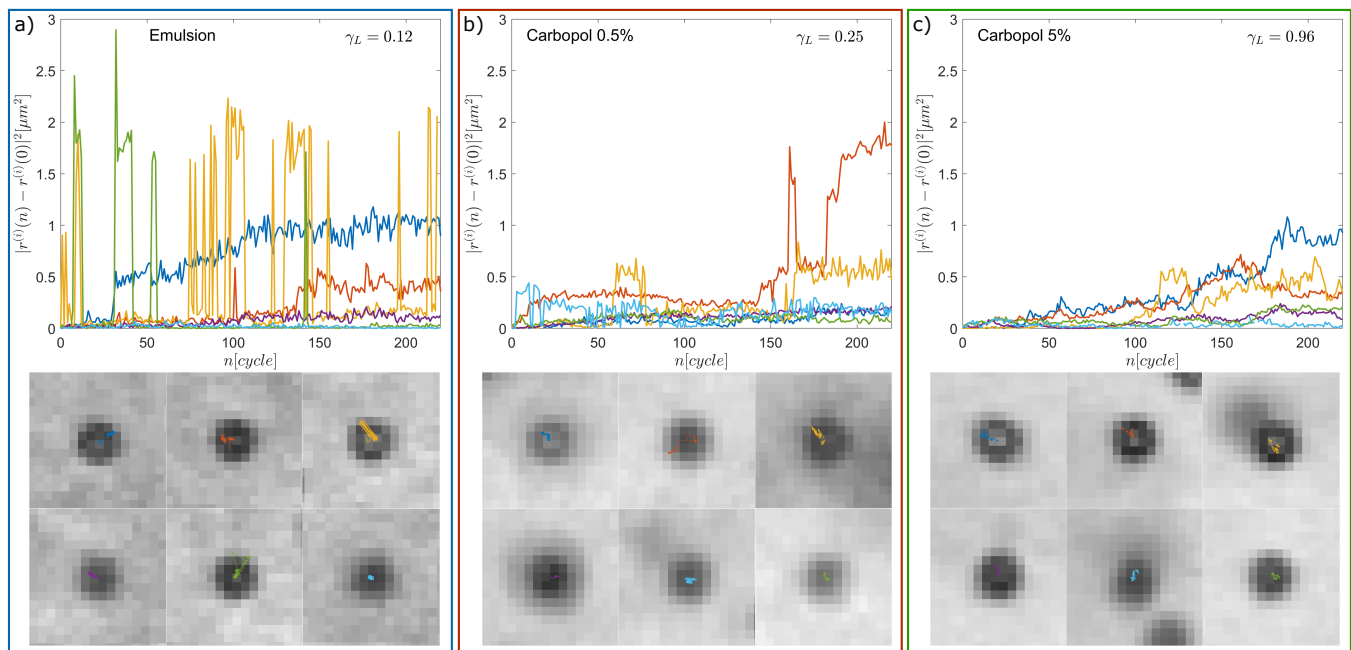


Fig. S10. Single particle trajectories for the three samples. Color scale is the same as in the main text. a-c) Top panel: time-resolved square displacement of representative particles trajectories during oscillatory shear for a given local strain amplitude $\gamma_L = 0.12, 0.25, 0.65$ for Emulsion, Carbopol 0.5% and Carbopol 5%, respectively. In the bottom panels, images of the particles shown in the respective upper panel, the colored lines mark the particle trajectories.

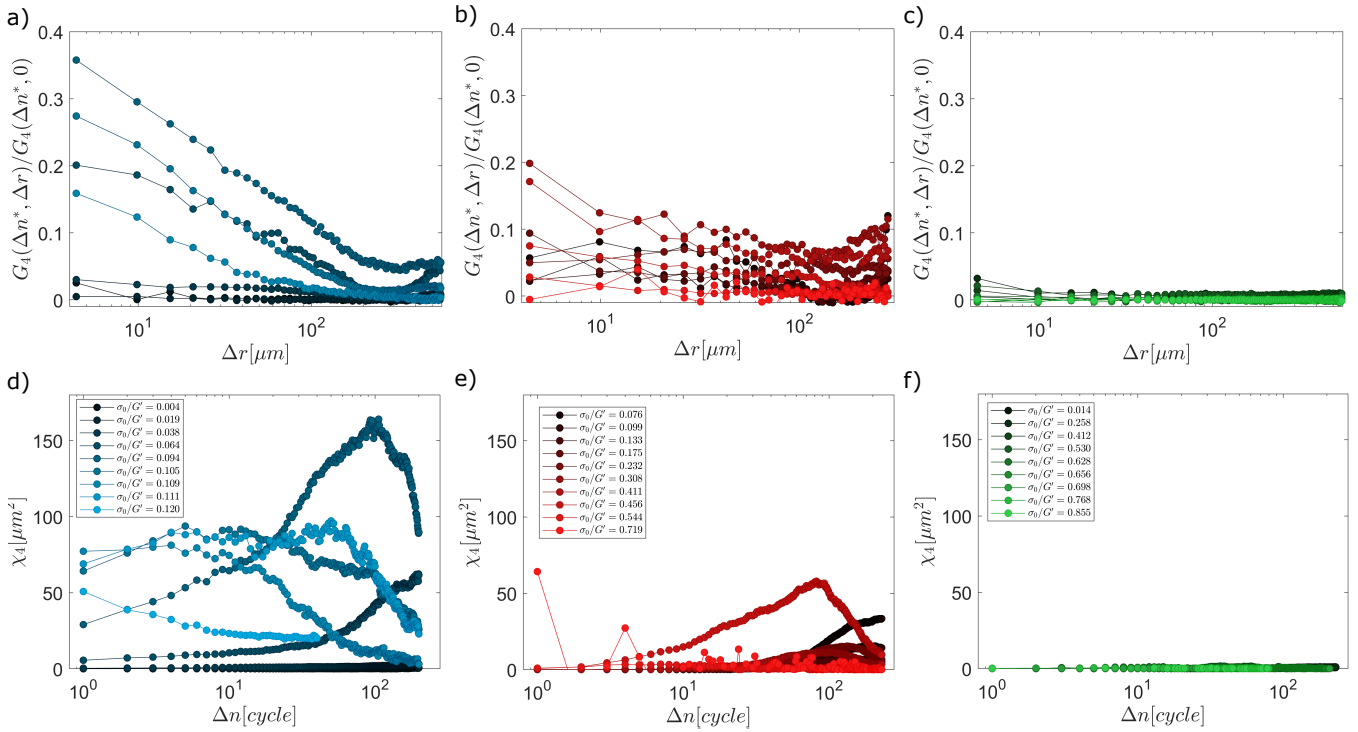


Fig. S11. Dynamical heterogeneity for the three samples. a-c) Normalized four-point correlator $G_4(\Delta r, \Delta n^*)$ as a function of the distance for the three samples, evaluated at Δn^* for which the $\chi_4(\Delta n)$ shows a peak. The different colors indicate different applied stresses, which increase from the darker to the lighter ones.